Visualizing Electrochemical CO_2 Reduction Reaction: Recent Progress of *In Situ* Liquid Cell Transmission Electron Microscopy

Zeyu Guo,[1] Paul Paciok,[2] Robert Zandonella,[2] Ziyun Xi,[1] Huiwen Zhu,[1] Pengyi Tang,[3,4,*] Pengfei Cao,[2,*] Joachim Mayer,[2,5] Jordi Arbiol,[6,7] Tao Wu,[1] and Mengxia Xu[1,*]

[1]Department of Chemical and Environmental Engineering, and New Materials Institute, University of Nottingham Ningbo China, Ningbo, 315100, China

[2]Forschungszentrum Jülich GmbH, Ernst Ruska-Centre for Microscopy and Spectroscopy with Electrons (ER-C), Forschungszentrum Jülich GmbH, 52425 Jülich, Germany

[3]National Key Laboratory of Materials for Integrated Circuits, Shanghai Institute of Microsystem and Information Technology, Chinese Academy of Sciences, Shanghai, 200050, China

[4]2020 X-Lab, Shanghai Institute of Microsystem and Information Technology, Chinese Academy of Sciences, Shanghai 200050, China

[5]Central Facility for Electron Microscopy (GFE), RWTH Aachen University, 52064 Aachen, Germany

[6]Catalan Institute of Nanoscience and Nanotechnology (ICN2), CSIC and BIST, Campus UAB, Bellaterra, Barcelona, Catalonia, Spain

[7]ICREA, Pg. Lluís Companys 23, Barcelona, Catalonia, Spain

*Corresponding author:
py.tang@mail.sim.ac.cn (P.Y. Tang), p.cao@fz-juelich.de (P.F. Cao), mengxia.xu@nottingham.edu.cn (M.X. Xu)

Abstract

The electrochemical carbon dioxide reduction reaction (CO_2RR) driven by renewable sources presents a promising avenue for converting CO_2 into valuable fuels and chemicals, thereby addressing both energy and environmental challenges. However, the development of high performance CO_2RR electrocatalysts has been impeded by a limited understanding of their dynamic evolution mechanisms, intrinsic stability factors, and activity origins under operational conditions. Transmission electron microscopy (TEM), with its nanoscale and atomic-level spatial resolution coupled with *in situ* microregional analyses, has emerged as an essential analytical tool in the study of heterogeneous electrocatalysis. *In situ* liquid cell TEM (LC-TEM) provides a powerful method for time-resolved monitoring of structural changes in catalysts during electrochemical CO_2RR. By correlating these observations with corresponding product distributions and electrochemical signals, it becomes feasible to elucidate precise structure-activity relationships and the intrinsic activation/deactivation mechanisms of electrocatalysts, thereby addressing the existing knowledge gap in electrochemical CO_2RR research. This critical review explores the evolution of *in situ* LC-TEM techniques and their applications in electrochemical CO_2RR research, focusing on three key aspects: the dynamic evolution of morphology and size effects, the dynamic identification of active sites, and the dynamic transformation of crystal structure and composition. Additionally, we evaluate the current challenges facing *in situ* LC-TEM and offer recommendations for its future advancement in electrochemical CO_2RR research.

Keywords: CO_2 reduction reaction; electrocatalysis, transmission electron microscopy; in situ TEM; liquid cell

1. Introduction

The Industrial Revolution has significant accelerated economic and industrial growth, albeit at the cost of increased fossil fuel dependence and excessive CO_2 emissions.[1,2] In response, there is a growing emphasis on utilizing renewable energy sources to drive CO_2 reduction and convert it into value-added chemicals, addressing pressing environmental and energy challenges.[3,4] The electrochemical CO_2 reduction reaction (CO_2RR) stands out among CO_2 utilization methods due to its mild operation conditions, high energy efficiency, tunable reaction kinetics, and flexible product distribution control.[5-7] Recent decades have witnessed significant advancements in CO_2RR performance. Sargent's group has extensively investigated Cu-based catalysts, achieving highly selective generation of multicarbon products in acidic electrolytes.[8-11] They demonstrated efficient CO_2 electrolysis at pH < 1, attaining 77% single-pass CO_2 utilization and up to 50% conversion efficiency for multicarbon products at 1.2 A cm^{-2} and 4.2 V full cell voltage.[9] Addressing industrialization challenges, Jiao and colleagues developed a tandem, kilowatt-scale CO_2 electrolyzer producing 98 liters of 1.2 M acetate with 96% purity with a total cell current of 300 A over 125 hours.[12] Concurrently, Han's team explored rare-earth metal integration with copper-based catalysts for multicarbon product generation under industrial current conditions.[13-16] Their Gd-doped CuO_x catalysts leveraged rare-earth metals' properties to stabilize active Cu^+ species and induce tensile strain for CO_2 activation, achieving a partial current density of 444 mA cm^{-2} at -0.8 V with 81.4% Faradaic efficiency for C_{2+} products.[15]

Despite significant advancements in CO_2RR performance, certain aspects of the reaction mechanisms remain elusive, primarily due to the complexity of multiple proton-coupled electron transfer steps and numerous reactive intermediates.[17-22] To address these challenges, various *in situ* characterisation techniques have been developed and applied. *In situ* Fourier transform infrared spectroscopy (FTIR) and Raman spectroscopy are frequently employed to monitor catalyst surface information and identify reaction intermediates, but suffer from water peak interference and low sensitivity, respectively. [23,24] *In situ* X-ray photoelectron spectroscopy (XPS) and X-ray absorption spectroscopy (XAS) provide

insights into element valence states and coordination environments, but are constrained by detection depth (1-10 nm) and averaged structural information.[25-27] In CO_2RR, the cathodic catalysts typically undergo reconstruction due to applied potentials.[28-38] Elucidating these structural changes is essential for comprehending CO_2RR mechanisms, as they correlate with catalyst activation/deactivation[36] and structure-activity relationships.[34] However, conventional *in situ* characterization techniques are limited in providing intuitive and precise information regarding alterations in catalyst morphology, components, valence states, and crystal structure during CO_2 electrolysis at atomic level. This limitation necessitates the development of more advanced analytical methodologies to fully elucidate the dynamic processes occurring during CO_2RR and to precisely tailor the synthesis of catalysts.

Transmission electron microscopy (TEM) provides high-resolution spatial information on catalyst structural changes during CO_2RR. Nevertheless, conventional *ex situ* TEM methods are limited in capturing dynamic catalyst evolution in real time and may misclassify active components due to post-electroreduction and re-oxidation. To address these limitations, advanced *in situ* TEM techniques have been developed to visualize these processes at atomic level. Identical location TEM (IL-TEM) bridges the gap between *ex situ* and *in situ* TEM, allowing observation of the same catalyst before/after different electrochemical test and study of various degradation mechanisms in electrocatalysis. While IL-TEM only captures pre- and post- reaction states, it provides insights into phenomena like support medium corrosion or aggregation due to weakened catalyst-support interactions. However, it cannot differentiate between migration, detachment/re-attachment, and dissolution/redeposition processes when observing the same catalyst.[39] Going one step further, *in situ* electrochemical liquid cell TEM (LC-TEM) systems leverage microelectromechanical system (MEMS) micromachining to fabricate a nano-laboratory within the sample stage, enabling time-resolved observations in liquid or gaseous environments incorporating heating and/or biasing the sample. For CO_2RR studies, potentials are applied through MEMS chips to simulate authentic CO_2 electrolysis conditions. When integrated with various state-of-the-art analytical techniques, such as electron energy loss spectroscopy (EELS)[40],

selected area electron diffraction (SAED)[41], and energy-dispersive X-ray spectroscopy (EDS)[42], these advanced *in situ* or operando LC-TEM or liquid cell scanning TEM (LC-STEM) methodologies provide valuable insights into dynamic structural evolution, structure-activity relationships and activation/ deactivation mechanisms in CO_2RR through direct visualization of the electrocatalytic processes.

This review critically evaluates the development and applications of *in situ* LC-TEM in heterogeneous catalysis, with a focus on recent CO_2RR studies. It delves into three key aspects: (1) dynamic evolution of morphology and size effects, (2) dynamic identification of active sites, and (3) dynamic transformations of crystal structure and composition. The review highlights the importance of understanding structure-activity relationships and activation/deactivation mechanisms of electrocatalysts using this technique. By addressing challenges in spatial resolution and electrochemical measurements, the review aims to improve imaging precision and accuracy of *in situ* LC-TEM studies. Additionally, it explores future directions for advancing this approach in electrocatalysis, including refinement of chip fabrication, development of advanced imaging technologies, and integration of machine learning. By providing time-resolved access to the chemical and structural information of catalysts during CO_2RR, *in situ* LC-TEM techniques offer valuable insights into catalyst stability and reaction mechanisms. The ongoing advancement of these methods is anticipated to greatly enhance our understanding of structure-activity relationships under real-time conditions, potentially leading to breakthroughs in the design and optimization of catalysts for more efficient and selective CO_2RR processes.

2. *In situ* LC-TEM for heterogeneous electrocatalysis

2.1 A concise overview of evolution of *in situ* LC-TEM

TEM, pioneered by Ernst Ruska and Max Knoll in 1933 (**Figure 1**), has revolutionized analytical capabilities in physics, materials science, and biology by surpassing optical microscopy's resolution limits.[43-45] *In situ* TEM techniques aim to directly observe nanomaterial transformation processes and

elucidate chemical reaction mechanisms at atomic level, facilitating the synthesis of materials that can be understood, controlled, and designed based on the inherent nature of chemical reactions.[46] Poppa's seminal work in the 1960s demonstrated *in situ* TEM's potential by enabling continuous observation of vapor-phase heterogeneous nucleation process of silver on amorphous carbon. [47] This research allowed direct measurement of absolute nucleation rates and precise nucleation size distribution functions.[47] Despite these advancements, TEM's high vacuum requirements hindered real-time observation of most heterogeneous reactions. The development of LC-TEM has provided researchers with a novel approach to investigate the real time microstructural evolution of substances in solution during chemical reactions, along with associated chemical and physical processes.[48-52] Notably, Parsons made significant contributions to the field in the 1970s by advancing imaging capabilities for inorganic and biological samples in liquid media. This was achieved through modifications to the environmental chambers, enabling the utilization of both "open cells" and "closed cells" configurations.[53]

In 2003, Ross et al. pioneered the integration of a microelectromechanical system (MEMS) into a custom-built electrochemical liquid cell for TEM imaging. [54] This cell, featuring two electrodes and two high flexural silicon nitride (SiN_x) electron transparent windows, enabled real-time observation of nanoscale Cu cluster nucleation and growth on gold wire during electrodeposition. The technique achieved a spatial resolution of approximately 5 nm and a temporal resolution of 30 frames per second, facilitating the visualization of solid-liquid interface reactions.[54] To address resolution limitations imposed by thicker liquid layers, Zheng et al. developed an improved SiN_x liquid cell in 2009, featuring a thinner solution layer of 200 nm confined between two SiN_x membranes with the thickness of 25 nm.[55] This design enhanced imaging resolution to the sub-nanometer scale, representing a significant progress in LC-TEM capabilities. This innovation enabled the first demonstration of platinum nanocrystals growth trajectories in liquids, allowing differentiation between monomer attachment and coalescence mechanisms.[55] In 2012, Yuk et al. introduced the graphene liquid cell to overcome limitations in electron transmittance, sensitivity and resolution caused by liquid thickness and

insufficient electron transmittance of SiN_x windows for higher atomic number elements. [56] This design achieved prolonged, high-resolution *in situ* imaging of platinum nanocrystal growth processes. Graphene's superior properties, including thinness, high mechanical tensile strength, and flexibility, were employed to encapsulate the growth solution under experimental conditions. Moreover, graphene's excellent heat and electrical conductivity render the liquid cell virtually immune to heating and biasing under electron beam irradiation, marking a breakthrough in *in situ* LC-TEM development.[57-61]

Initial *in situ* LC-TEM experiments were limited by the absence of a heating reaction chamber. Chee et al. addressed this by developing a liquid cell with heating capabilities, comprising a heater top chip (50 nm-thick SiN_x window) and a bottom chip (25 nm-thick SiN_x window).[62] This innovation enabled direct *in situ* observation of the nanoscale Kirkendall effect during electrochemical substitution reactions, demonstrating hollow nanostructure formation mechanism.[62] These advancements provided valuable insights into heterogeneous electrochemical reactions, facilitating time-resolved tracking of catalyst structure and morphology evolution, and exploration of reaction mechanisms and structure-activity relationships.[33,63-67] The application of *in situ* LC-TEM to electrochemical CO_2RR studies has gained prominence since 2020. Arán-Ais et al. conducted pioneering experiments using a liquid and biasing holder with a flow cell chip to address the limited understanding of the stability of tailored nanostructures, such as cubic Cu_2O, under reaction conditions. [32] This setup employed continuous electrolyte delivery to the microfluidic cell via a pump, with real-time electrochemical performance analyzed using a potentiostat connected to the holder. The study visually demonstrated catalysts' highly dynamic properties during CO_2 electrolysis, including mobility and reconstruction processes, highlighting *in situ* LC-TEM's advantages in elucidating electrochemical synthesis mechanisms and monitoring catalyst performance during electrocatalysis.[28,32] Subsequently, *in situ* electrochemical LC-TEM has undergone rapid development in CO_2RR research. The typical experimental setup for these studies utilizes a three-electrodes electrochemical liquid cell encapsulated in a holder between two SiN_x windows.[28-32,34-38]

Despite the significant progress in electrochemical *in situ* LC-TEM techniques for CO_2RR, the presence of a liquid electrolyte continues to pose challenges for directly probing atomic dynamics at the solid-liquid interface under operando conditions. In 2024, Zhang and co-workers developed a polymer electrochemical liquid cell to enable time-resolved observation of atomic dynamics in CO_2RR. This innovation facilitated the first atomic-scale observation of the formation and dynamics of amorphous transition layers on metallic copper catalyst surfaces during CO_2 electrolysis. This study not only reveals the dynamic atomic structure of the electrified solid-liquid interface but also established critical structure-activity relationships, thus laying the foundation for precise control of various electrochemical reactions.[68]

2.2 *In situ* LC-TEM imaging techniques for electrochemical CO_2RR

Currently, the study of CO_2RR using *in situ* LC-TEM faces several challenges due to the reaction's three phase (gas-liquid-solid) nature and the requirement for potential-controlled processes. The primary difficulties include: (1) maintaining an appropriate thickness in the projection direction, as TEM samples must be electron-transparent, ideally within 50 nanometers[69-71], which is difficult to achieve for observations involving aqueous-phase CO_2RR; (2) ensuring compatibility with the vacuum environment, since the high vacuum conditions of the TEM column ($\leq 10^{-5}$ Pa)[72-74] are incompatible with most liquid electrolytes used in CO_2 electrolysis due to their high saturated vapor pressures. These factors significantly affect image quality and the accuracy of data analysis during visualized CO_2 electrolysis. Consequently, this section examines the evolution of *in situ* LC-TEM imaging techniques developed to address these challenges and enable the visualization of electrochemical CO_2RR processes (**Figure 2**).

Early *in situ* LC-TEM imaging approaches utilized thin samples of ionic liquids with low vapor pressures to overcome the challenges associated with liquid-phase imaging in high vacuum environments.[75-78] A significant advancement in this field was made by Mizoguchi and Miyata in 2017, who developed a

sample preparation method for liquid thin film samples suitable for STEM-EELS observation.[79] Their technique, which combined ionic liquid 1-ethyl-3-methylimidazolium bis(trifluoromethyl-sulfonyl) imide (C_2mim-TFSI)) and ethanol and deposited the solution onto a thin, porous solid film using a pipette, enabled the fabrication of liquid-only layers with thicknesses ranging from one to tens of nanometers within an open cell (**Figure 2a**). This method is promising to facilitate high spatial resolution studies of chemical reactions, ionic behaviors, and local structures in liquids.[79] Ionic liquids have garnered attention as potential electrolytes for CO_2RR due to their electrical stability, high ionic conductivity, high CO_2 solubility, and a wide electrochemical window.[80,81] However, the application of this liquid-phase TEM imaging technique for visualizing CO_2 electrolysis remains limited. The primary constraints include the high cost and potential environmentally toxicity of ionic liquids, exemplified by tetrafluoroborate's decomposition to hydrogen fluoride, which poses challenges for commercial CO_2 electrolysis applications.[82] Additionally, the high vacuum environment of the TEM column causes CO_2 dissolved in ionic liquids to overflow, impeding effective CO_2 electrolysis.

An alternative open LC-TEM imaging technique is environmental TEM (ETEM), which is capable of managing the intrinsic vapor pressure of the liquids used.[63,83-85] ETEM maintains a relatively higher pressure in the sample chamber (up to 2 kPa) compared to the rest of the microscope, achieved through differential pumping, as illustrated in **Figure 2b**.[52,86,87] This approach has been applied in studies of metal-air batteries [88-90] and used to examine transformations in electrode materials during the operation of lithium-ion batteries.[91] Despite these advancements, challenges persist for CO_2 electrolysis under harsh conditions using open ETEM. The precise control of droplet states in ETEM experiments remains difficult. While ETEM provides a near-atmospheric pressure environment within the specimen chamber, electrolyte solutions with high vapor pressures may still evaporate, leading to salt precipitation. Additionally, the gaseous products generated during the CO_2RR process can be removed by the vacuum, complicating the establishment of relationships between the generated products and the reactions, electrocatalyst changes, and its degradation. These limitations collectively

hinder the widespread application of the open ETEM technique for liquid-phase CO_2RR analysis.

In contrast to the open-cell strategies previously discussed, closed liquid sample chambers have been developed to maintain higher pressures in the specimen environment. These microchip liquid cells are specifically designed to meet the requirements of visualizing CO_2 electrolysis. As illustrated in **Figure 2c**, closed electrochemical liquid cells with three-electrode MEMS chips provide both liquid isolation and TEM imaging capabilities essential for visualizing CO_2 electrolysis studies.[91-94] Several TEM device manufacturers, including DENSsolutions, Hummingbird, Protochips, Zeptools and Insight Chips, have introduced analytical TEM holders with MEMS chips for *in situ* electrochemical analysis. This innovation enables time-resolved monitoring of catalysts during the CO_2RR process and allows for the adjustment of applied electrical signals to simulate actual CO_2RR conditions via MEMS. Consequently, existing *in situ* TEM studies for CO_2RR have predominantly employed closed liquid cell strategies with MEMS chips.[28-38]

Building upon the closed liquid phase TEM imaging technique, graphene liquid cells have demonstrated efficacy in preserving volatile samples, such as biological cells and liquid crystals within the ultra-high vacuum environment of TEM.[56-59,61] As shown in **Figure 2d**, graphene can be suspended over grid apertures, providing coverage across the entire grid. The low atomic number of carbon atoms in graphene results in minimal interaction with the electron beam, leading to enhanced image sharpness.[56,58,95] This characteristic enables high-resolution *in situ* observations under liquid conditions. However, graphene liquid cells face several limitations in visualizing CO_2 electrolysis. These include complex assembly procedures, restricted liquid mobility, and an extremely low liquid cell capacity. In contrast to the nanoliter capacity of microchip liquid cells, graphene liquid cells can encapsulate and image less than 0.01 picolitres of liquid.[49] This ultra-small capacity constrains the design of electrode patterns and the application of cathode bias. Furthermore, the chemical inertness of graphene renders it less reactive than amorphous carbon substrates at lower accelerating voltages.[96] These limitations

underscore the need for continued development of *in situ* LC-TEM techniques for CO_2 electrolysis studies, balancing the advantages of high-resolution imaging with the practical requirements of electrochemical experiments.

3. Applications of *in situ* LC-TEM for electrochemical CO_2RR

Techno-economic analyses of commercial CO_2 electrolysis processes suggest that the Faradaic efficiency (FE) for C_1 products (e.g., CO and formate) must exceed 90% at industrial current densities (>200 mA cm^{-2}) to be economically viable.[97] However, the reported operating times for CO_2 electrolysis with stable FE typically do not exceed 1000 hours, which is significantly less than the approximately 100 days required for initial prototype electrolyzer testing and the 50,000-hour lifespan necessary for commercial CO_2 electrolysis processes.[98,99] This discrepancy underscores the urgent need to investigate the intrinsic stability of CO_2RR, including structure-activity relationships and activation/deactivation mechanisms, to ensure long-term efficient CO_2 electrolysis. A comprehensive study[100] has identified general deactivation modes of electrocatalysts for CO_2RR, including aggregation[101], coalescence[102], adsorbate-induced atom mobility[103], segregation[104], defect formation[105], dissolution[106], fragmentation[32], Ostwald ripening[36], self-inhibition[107], impurity effect[108], cocatalyst depletion[109], detachment[110], and self-poisoning[111,112]. These deactivation modes are typically associated with structural evolution of the catalyst, emphasizing the importance of conducting *in situ* electron microscopy studies to visualize the dynamic changes in heterogeneous CO_2RR catalysis.[24,86,94,113-116] To provide a structured overview of existing studies applying *in situ* LC-TEM techniques to CO_2RR, we classify and discuss them according to three main categories: morphology and size effect, active sites, and dynamic changes in crystal structure and composition.

3.1 Dynamic evolution of morphology and size effect

Establishing credible structure-activity relationships in CO_2RR necessitates time-resolved tracking of dynamic structural changes on electrocatalyst surfaces, linking these changes (e.g., morphology and

size) to electrocatalytic performance.[115,117-119] Cu-based catalysts are widely recognized for enabling deep electrochemical reduction of CO_2 to multicarbon products, attributed to their negative adsorption energy for adsorbed CO (*CO) and positive adsorption energy for adsorbed hydrogen (*H), facilitating a deeply coupled process involving multiple proton and electron transfers.[19,120-123] However, the stability and morphological evolution of catalysts, particularly oxide-derived Cu-based catalysts with tailored nanostructures, under CO_2 electrolysis conditions remain poorly investigated.[124-129] Cu-based catalysts' electrocatalytic performance is highly sensitive to surface structure and treatment. Under applied potential, electrocatalysts undergo reconstruction, primarily influenced by cathodic material and electrolyte properties.[130-133] Therefore, understanding their stability and morphological evolution is crucial for the rational design of the optimal electrocatalysts for CO_2RR.

Arán-Ais et al. conducted a comprehensive investigation into real-time structural changes of cubic Cu_2O with (100) facet during CO_2 electrolysis using STEM.[32] The study utilized a liquid biasing holder and a flow-cell chip equipped with a SiN_x window and three Pt electrodes (**Figures 3e-g**) to capture *in situ* STEM images at various time points (1 s, 61 s, 246 s, and 750 s) as illustrated in **Figures 3a-d**. To mitigate electron beam-induced artifacts, the researchers employed a low electron dose rate of approximately 20 e^- nm^{-2} s^{-1} for *in situ* LC-STEM experiments. At this dose rate, CO_2RR remained unaffected by electron beam irradiation, with sample reorganization observed only upon application of a working potential. Upon applying a potential of −0.7 V vs. reversible hydrogen electrode (RHE) to the cubic Cu_2O, minimal changes were observed during the initial stage (1-61 s), except for slight positional shifts of loosely attached cubic Cu_2O (**Figures 3a and b**). As the chronoamperometry (CA) progressed (61-750 s), a notable decrease in cubic Cu_2O size was observed, accompanied by the emergence of new structures, some displaying dendritic morphology (**Figures 3c and d**). This transformation may be attributed to variations in surface energy covered by different intermediates, resulting in the formation of specific facets during *in situ* reconstruction of the cubic Cu_2O surface. This research provides valuable insights into the intrinsic stability of electrocatalysts with specific

nanostructures. Importantly, the *in situ* TEM studies investigated the persistence of anticipated favorable catalyst structures during dynamic CO_2 electrolysis and their influence on the electrocatalytic selectivity and activity trends. Through this approach, the researchers successfully achieved time-resolved imaging of morphological features and unveiled the evolution of electrocatalytic selectivity and activity during CO_2RR.

Subsequently, Grosse et al. systematically delved into the reconfiguration process of cubic Cu_2O during CO_2 electrolysis, considering varying particle sizes and loadings.[31] The study encompassed catalyst detachment, redeposition, fragmentation, and aggregation. *In situ* experiments were conducted using a high-capacity electrochemical LC-TEM holder equipped with an Ag/AgCl reference electrode (RE) and a Pt counter electrode. The researchers correlated morphological changes with electrocatalytic efficiency and reaction selectivity by analyzing electron selectivity trends for various gaseous products using online gas chromatography (GC), with a time resolution of approximately 17 minutes. Live-recorded images revealed that both larger (390 nm and 170 nm) and smaller (80 nm) cubes underwent fragmentation and size reduction upon application of reduction potentials. Larger cubes (390 nm and 170 nm) exhibited no significant positional migration and maintained a stable framework from 0 to 45 minutes under an applied potential of −0.9 V vs. RHE (**Figures 3h-k and l-o**). In contrast, smaller cubes (80 nm) demonstrated poor stability, evidenced by degradation and substantial reduction in quantity upon electrolyte introduction (**Figures 3p-s**). The researchers employed a combination of *in situ* TEM imaging and on-line GC detection to investigate time-resolved structure-activity relationships (**Figure 3t**). Over a 12-hour period at −1.1 V vs. RHE, the selectivity for C_2H_4 and CH_4 products from three cubic Cu-based catalysts gradually diminished under CO_2RR conditions, attributed to degradation in cubic catalyst morphology. Notably, 80 nm sized cubic particles exhibited a sharp decline in selectivity for hydrocarbon products (C_2H_4 and CH_4) from 0 to 6 hours while sustaining high partial current density for CO. Additionally, their activity and selectivity for the hydrogen evolution reaction (HER) increased significantly from 8 to 12 hours. This phenomenon may stem from the instability of the nanocubes

during CO_2 electrolysis, leading to degradation and detachment from the working electrode surface (**Figures 3p-s**).

While *ex situ* studies have demonstrated the dynamic evolution of Cu-based catalysts under applied potential and its impact on CO_2RR performance, these findings are inherently limited due to the cessation of electrochemical operations and removal of potentials prior to analysis. In contrast, *in situ* LC-TEM techniques offer valuable real-time insights into the optimal kinetic morphology endpoints of Cu-based catalysts throughout CO_2 electrolysis processes. Wang et al. employed a novel one-step approach to fabricate 2D Cu(II)O nanosheets (NS), enabling multicarbon product generation via CO_2 electrolysis at industrial-scale current densities under neutral electrolytic conditions.[29] The study utilized TEM with imaging, diffraction, and other techniques to elucidate CuO NS recombination during CO_2RR (**Figure 4**). A Poseidon Select electrochemical cell holder (Protochips, *in situ* TEM E-chip cell with 3-electrodes) maintained the ultrathin liquid electrolyte layer and liquid chamber. The researchers initially investigated the morphological evolution of CuO NS as the cathode under open circuit potential (OCP) conditions in 0.1 M CO_2-saturated $KHCO_3$ solution. *In situ* TEM images revealed that within 50 s of OCP application, CuO NS (approximately 300 nm in width) fragmented into smaller flake fragments (**Figures 4a-b**). From 50 to 110 s, fragmentation continued, with smaller fragments desorbing from the working electrode and eventually disappearing (**Figures 4b-c**). Subsequently, the application of −0.84 V vs. RHE enabled real-time monitoring of the fragmented Cu-based catalyst's morphological evolution (**Figure 4d**). During 0-200 s, some fragments gradually agglomerated (red circles), while others disappeared from the view (cyan circles) (**Figures 4e-h**). After 8 and 16 minutes of applied bias, Cu flake fragments acting as "building blocks" aggregated into spherical shapes, ultimately forming branching dendritic structures as the final stable catalyst morphology (**Figures 4i-l**). This work elucidated the morphological transformation pathway of Cu-based catalysts, progressing from nanosheets to highly active nanoscale flake fragments, and ultimately aggregating into dendric Cu structures resembling trees. Through real-time imaging, the study successfully captured the final

stable electrocatalyst morphology under flowing CO_2 electrolysis conditions. Notably, the growth mechanism could only be comprehensively understood through real-time morphological analyses facilitated by *in situ* TEM techniques, highlighting the limitations of traditional *ex situ* methodologies.

3.2 Dynamic identification of active sites

In situ observations of catalyst dynamics during CO_2 electrolysis provide a robust framework for the precise identification of active sites and the acquisition of crystal structure dynamics information. This approach offers an effective strategy for advancing the development of high-performance catalysts in CO_2RR, while simultaneously facilitating the establishment of structure-activity relationships.[134-137]

Single-atom catalysts (SACs), characterized by precisely defined coordination structures and uniformly controllable active sites, present an ideal platform for exploring structure-activity relationships.[138-142] Hsu et al. pioneered the application of *in situ* electrochemical LC-TEM, enabling real-time monitoring of structural transformations in Cu SACs during CO_2 electrolysis (**Figures 5a**).[30] The preparation process for *in situ* electrochemical LC-TEM involved initial dispersion of as-prepared Cu SACs in ethanol. Subsequently, the catalyst ink was drop-cast onto an electrochemical chip equipped with three platinum (Pt) electrodes designated as working, counter, and reference electrodes. Another electrochemical chip window was positioned at the bottom to create a sealed ultra-thin liquid layer, isolating it from the vacuum environment within the TEM column (**Figures 5b**). Electrolyte injection through the observation window was performed at a flow rate of 300 μL h^{-1}, maintaining a thickness of approximately 500 nm to mitigate the risk of air bubble aggregation. At a constant potential of −1.83 V vs. a Pt reference, the characteristics of SACs on the working electrode remained indiscernible during the initial reaction stage (0-40 s) due to the limited mass scattering contrast of individual atoms within the liquid layer (**Figures 5a1-a2**). However, during the reaction period from 80 to 120 s, TEM images revealed an increased number of bright spots, approximately 2.6 nm in size (highlighted in orange circles), indicating Cu cluster formation (**Figures 5a3-a4**). The Cu clusters subsequently grew to about

3 nm before ceasing growth, confirming that the bright spots were attributable to Cu cluster formation rather than redeposition (**Figure 5a5**).

The Integration of *in situ* TEM imaging with operando spectroscopies elucidates that the morphological alterations observed in Cu SAC during CO_2 electrolysis stem from potential-driven recombination. Notably, operando X-ray absorption/emission spectroscopy unveils that this phenomenon is closely linked to Cu-N coordination bonds.[30] These findings demonstrate that coordination recombination in SACs triggers an adaptive dynamic low-coordinated conformation, enabling exceptional activity and selectivity for the electrochemical CO_2RR-to-CO process. Consequently, we advocate for the combination of *in situ* TEM techniques with more advanced characterization methods to obtain comprehensive information during CO_2 electrolysis, particularly emphasizing time- and energy-resolved methods. Typical characterization methods suitable for integration with *in situ* TEM techniques include XAS[143], XRD[144], and XPS[23]. These techniques provide evidence for the identification of dynamically changing coordination environments, crystal structures, and valence information of electrocatalysts, respectively.

While significant progress has been made in advancing Cu-based electrodes for the electrocatalytic conversion of CO_2 to C_{2+} products, enhancing C-C coupling efficiency and understanding the relevant reaction mechanisms remain crucial challenges in the field of CO_2 electrolysis.[145-149] Li et al. employed a comprehensive approach which integrates *ex situ* electron microscopy, chemical passivation techniques, and *in situ* electrochemical LC-STEM to uncover and analyze critical information regarding the active sites on Cu-based catalysts in CO_2 electrolysis, focusing on their morphology and crystal structure.[28] As illustrated in **Figures 5c**, initial *ex situ* structural characterization of Cu nanoparticles (Cu NPs) used as cathodic catalysts, both before and after CO_2 electrolysis, revealed a significant morphological transformation at approximately 50 s, leading to the appearance of previously unobserved cubic structures. During the subsequent minutes of CO_2 electrolysis, the material

reconstructed into derived cubic Cu-based catalysts (**Figures 5d**). Further investigation through HRTEM and selected area electron diffraction (SAED) indicated that the resulting cubes were monocrystalline Cu_2O cuboids (**Figures 5e**). The phenomena of oxidation and crystallization observed in *ex situ* SEM stem from the behavior of Cu NPs transforming into a highly reactive disordered state upon the application of cathodic bias. Upon releasing the biasing voltage, this reactive state gradually stabilizes, facilitating oxidation and crystallization under ambient conditions.

Despite the observation of small particles derived from Cu NPs, monocrystalline Cu_2O cuboids, and their reduced equivalents, these entities were insufficient to be considered as the active phase for CO_2RR-to-C_{2+} process. To pinpoint the active phase, Li and co-workers utilized chemical immersion to introduce the passivator benzotriazole (BTA), aiming to prevent Cu oxidation in the surrounding environment.[150] The findings revealed that the highly active disordered state of Cu NPs, formed through electrochemical reconstruction, optimized the binding of catalytic intermediates on their surfaces, thereby enhancing the C-C coupling efficiency for efficient CO_2RR-to-C_{2+} process. To rule out the possibility of monocrystalline Cu_2O cuboids as the active phase, *in situ* electrochemical LC-STEM was employed to monitor the dynamic evolution of Cu NPs under cathodic bias. The entire assembly, comprising a 500-nm liquid layer and a SiN_x window with the thickness of 100 nm, was designed to enhance TEM imaging resolution. Additionally, the electrolyte purge was halted during the bias process to obtain higher quality structural information from the catalyst with improved accuracy. As shown in **Figures 5f**, under a negative bias potential of −0.6 V vs. the internal reference electrode (C/Pt) in 0.1 M $KHCO_3$ electrolyte, irregular smaller Cu nanoparticles (~7 nm) transformed into a disordered Cu structure (~20 nm) within just one second. In contrast, larger Cu NPs (15-20 nm) did not exhibit similar morphological changes under identical conditions (**Figures 5g**). Furthermore, it was observed that the precursor Cu nanoparticles (~7 nm), due to their higher surface energy, experienced significant atomic migration upon electrochemical perturbations, leading to a high concentration of disordered structures serving as catalytic sites. This investigation confirmed that the active phase was the ~20 nm

disordered Cu phase, formed within a few seconds by fusion, while the formation of Cu_2O cuboids occurs exclusively at open circuit. Consequently, determining the active phase in CO_2RR cannot solely rely on post-reaction catalyst structure characterization. Given the inherent instability of active sites, a comprehensive combination of characterization techniques is imperative for accurate identification.[27,94,115,118,119,151-153]

Yang's research team extended the investigation by Li and co-workers through the application of operando electrochemical LC-STEM and four-dimensional STEM (4D-STEM) techniques (**Figure 6a**).[34,37,154,155] The 4D-STEM technique provides image, orientation and strain information to investigate the morphology and structural dynamics of the catalyst during the reaction process by recording a two-dimensional electron diffraction pattern over a 2D grid of probe positions.[34] This integrated approach aimed to validate the presence of metallic copper nanograins, utilizing 7-18 nm Cu NPs as a model catalyst. Their findings provided critical insights for elucidating the true origin of active sites. Operando electrochemical LC-STEM allows for the real-time tracking of changes in the morphology and crystal structure of Cu at the nano-scale in liquid phase, while preserving electrochemical reaction conditions.[34] The beam dose during the *in situ* electrochemical LC-STEM experiments was approximately 12.5 e^{-} nm^{-2} s^{-1}, thereby preventing beam-induced damage.

As depicted in **Figure 6b**, substantial aggregation of Cu NPs was observed after a single LSV scan from 0.4 V to 0 V vs. RHE. Images acquired through operando electrochemical LC-STEM at the same location with a potential of 0 V vs. RHE revealed that the initial 7 nm Cu NPs had aggregated into larger particles ranging from 50-100 nm in size (**Figures 6c-d**). Following the initial LSV scan, applying a potential of 0 V disclosed rapid structural transformations of the Cu NPs, leading to the formation of new Cu NPs and additional particle growth (**Figures 6e-h**). At the optimal potential for CO_2RR-to-C_{2+} products (−0.8 V vs. RHE), pronounced particle migration was observed within the first 8 s, followed by progressive particle aggregation between 8-32 s (**Figures 6i-l**). Collectively, the operando electrochemical LC-STEM

analysis of the 7 nm Cu NPs identified two distinct morphological types: loosely connected small Cu NPs and tightly packed large Cu NPs, which may function as active sites for CO_2RR. However, detailed crystallographic information on these structures remains lacking.

Consequently, a significant advancement in this work was achieved through the application of *in situ* liquid-phase 4D-STEM. At potential of 0 V vs. RHE, the 7 nm Cu NPs formed loosely connected structures with nanograins. As shown in **Figure 6m**, the virtual 4D-STEM image reconstructed from three diffraction spots distinctly reveals the highly polycrystalline nature of active copper, characterized by finely dispersed nanoparticles. Two distinctive regions were identified, delineating nanoparticle boundaries with either loose connections (**Figure 6n**) or tight overlapping (**Figure 6o**). The initial 7 nm Cu NPs served as foundational units for establishing nanoparticle boundaries, which may become enriched with defects and dislocations following the initial phase of electrolysis at 0 V. False-color dark-field 4D-STEM images, based on three diffraction points shown in **Figure 6p,** illustrated that most Cu NPs consist of individual particles separated by grain boundaries and/or stacking layers (**Figure 6q**, white arrows). This study also indicated that the initial aggregation and formation of nanograins in 10 nm and 18 nm Cu NPs were less pronounced compared to those observed in 7 nm Cu NPs, resulting in lower nanoparticle boundary densities and reduced activity at under-coordinated Cu sites.

Furthermore, *in situ* X-ray spectroscopic characterization confirmed that the coordination number at polycrystalline copper nanocrystalline boundaries was approximately 8, indicating that the formation of polycrystalline nanograins can create active copper sites with low coordination numbers. By employing appropriate operando characterization techniques and analyzing *in situ* TEM images, the researchers were able to establish a structure-activity relationships between the low coordination sites on Cu NPs and their performance in electrochemical CO_2RR process.[156] These quantitative structure-activity relationships, which can be accurately determined only through *in situ* characterizations,

contribute to the precise regulation of catalytic activity and selectivity and facilitate the development of efficient CO_2RR catalysts.

In the context of CO_2RR, electrified solid-liquid interfaces (ESLIs) play a crucial role in facilitating electron and proton transfer, which can significantly alter catalyst structure and, subsequently, influence reaction pathways and product distributions. While ESLIs are fundamental for the thermodynamic and kinetic processes of these reactions, directly probing the atomic dynamics at solid-liquid interfaces under electro-biasing conditions remains a significant challenge. This limitation primarily stems from the extremely limited spatial resolution at the atomic scale when conducting *in situ* TEM imaging through liquid electrolytes. To address this challenge, Zhang et al. developed an innovative electrochemical polymer liquid cell (PLC) which enables direct, high-resolution monitoring of atomic dynamics at ESLIs during Cu-catalyzed CO_2 electrolysis.[68] The PLC substrate comprises two commercial copper TEM grids: a complete bottom grid and a top-truncated grid with truncated lengths of 0.5-1.0 mm and 200 mesh squares. The top grid was coated with a layer of aluminum oxide on both sides via sputtering, followed by the transfer of a 10 nm thick formvar polymer film onto one side. The bottom grid underwent a similar process, with an aluminum oxide layer sputtered on both sides, followed by the sequential deposition of a 10 nm formvar polymer film and a 10 nm thick Pt electrode through electron beam evaporation. The experimental setup involved loading Cu nanowires (NWs) suspended in CO_2-saturated 0.1 M $KHCO_3$ electrolyte onto the bottom grid, which was then assembled with the top grid to form the electrochemical PLC (**Figure 7a**). This assembly was subsequently mounted into a custom-made electrical biasing TEM holder, allowing for the application of potential and the conduct of a visualized CO_2RR study.[68]

Upon application of a −1.1 V vs. RHE potential, the Cu NWs' surface exhibited irregular fluctuations between 0 and 3.2 s, with a distinct amorphous phase interface emerging at 0.8 s (**Figure 7b**). This perturbed amorphous structure demonstrated periodic appearance and disappearance, vanishing at

1.6 s and reappearing at 3.2 s. Additionally, EELS and EDS analyses indicated that the amorphous interphase comprised a complex containing both Cu^0 and Cu^{+1}. The authors attributed the oxidation of Cu NWs under cathodic currents to the spontaneous degradation of the $[CuCO]^+$ complex, formed from dissolved Cu species and CO from adsorbed molecules in solution, ultimately yielding Cu^+ and CO. Further analysis of *in situ* TEM imaging revealed two dynamic behaviors of intermediate species affecting the amorphous interface reconstruction (**Figures 7c**). Firstly, the liquid amorphous structure flowed along the crystalline Cu surface, moving from left to right and eventually disappearing from view between T_0 and T_0 + 3.0 s (**Figure 7d**). Secondly, an interconversion process between crystalline and amorphous components was observed from T_0 to T_0 + 4.0 s. The amorphous interface gradually dissolved into the crystalline Cu from T_0 to T_0 + 2.8 s. However, from T_0 + 2.8 s to T_0 + 4.0 s, the crystalline Cu began replenishing the amorphous interface, leading to a rougher surface (**Figure 7e**).[68]

This innovative PLC design not only enhances *in situ* LC-TEM resolution to the atomic level but also minimizes electrolyte addition by forming numerous small liquid pockets within the PLC, thus avoiding the window bulging problem common in SiNx liquid cells. Furthermore, PLC can be rapidly cooled using cryogenic TEM techniques, enabling immobilization of active reactive species and structures for subsequent EELS and EDS characterizations. *In situ* PLC TEM offers promising perspectives for studying atomic mechanisms of electrocatalysis at angstrom-scale resolution. However, this setup requires optimization for long-term reaction observations, as it cannot replenish the electrolyte through liquid flow. When conducting extended CO_2RR stability studies, challenges such as product accumulation, gas bubble formation, local pH changes, and decreased CO_2 concentration may arise in this configuration.

3.3 Dynamic transformations of crystal structure and composition

Recent studies on CO_2RR have demonstrated that electrocatalysts undergo phenomena such as recrystallization and surface reconstruction during the reaction processes.[157-159] Additionally, multi-component catalysts experience changes including segregation, phase separation, and loss of active

components. These processes lead to alterations in the chemical composition and properties of the catalysts, ultimately resulting in diminished catalytic activity or complete deactivation.[160-163] To address these issues, *in situ* LC-TEM techniques have been employed to elucidate the dynamic changes in the crystal structure and composition of electrocatalysts during CO_2 electrolysis. The goal is to design high-performance catalysts and to understand the mechanisms of activation and deactivation.

Vavra et al. developed a customized *in situ* TEM electrochemical chip that incorporates a genuine glassy carbon working electrode. This experimental setup allowed for real-time monitoring of the electrochemical mechanisms underlying the activation of Cu-based catalyst during the initial stages of CO_2RR.[36] As shown in **Figures 8a-c**, a three-step *in situ* electrochemical scheme using 7 nm Cu nanospheres as the model was designed: starting from OCP, followed by a short LSV interval, and finally maintaining a constant potential (**Figures 8d**). During *in situ* LC-TEM experiments, the structure and size of the Cu nanospheres remained unchanged throughout the LSV interval from OCP to −0.25 V vs. RHE (−10 s to 0 s) (**Figures 8a**). However, during the subsequent 60 s chronoamperometry experiment at −0.25 V, it was observed that some primary particles (highlighted in red) grew into larger secondary particles (**Figures 8b**). In contrast, other nearby dispersed primary particles (highlighted in blue) exhibited a noticeable reduction in size or vanished altogether (**Figures 8c**). The area-weighted particle size distribution plots indicated that the average particle size within the field of view remained constant, despite a reduction in the number of primary particles and an increase in the number of secondary particles (**Figure 8e**). This phenomenon can be attributed to a net reduction in surface free energy. The high free energy associated with smaller-sized particles leads to their dissolution under applied potential (−0.25 V vs. RHE). However, this dissolution is compensated by the growth of secondary particles, ultimately achieving a more stable state (**Figure 8f**).

Interestingly, to complement the monitoring of the crystal structure, *in situ* SAED patterns were recorded in the same electrochemical experiments to determine the structural changes in the initial

stages of the CO_2RR (**Figure 8g**). *In situ* diffraction patterns of Cu_2O were recorded at 0.4 V vs. RHE (**Figure 8h**), while diffraction patterns of Cu were recorded at −0.1 V and −0.8 V vs. RHE (**Figures 8g and i**). The full *in situ* SAED pattern reveals that the reduction of Cu_2O to Cu is effectively accomplished during LSV scans down to −0.2 V vs. RHE (**Figures 8j-l**). The integration of *in situ* LC-TEM and SAED elucidates the dissolution/redeposition mechanism and crystal structure alterations of Cu nanospheres under initiation and constant applied potential, offering a new perspective on establishing structure-activity relationships. in CO_2 electrolysis.[164-167]

Non-metallic dopants, such as halogens, incorporated into Cu-based catalysts have demonstrated remarkable activity and selectivity in the electrochemical CO_2RR, yielding highly specified C_{2+} hydrocarbons.[168-174] Nevertheless, further elucidation is needed regarding the loss of halogen atoms at electrochemical reduction potentials and the dynamic transformation of compositions. Yoon et al. employed *in situ* electrochemical LC-TEM in STEM mode, featuring a Pt counter electrode and an Ag/AgCl (3 M KCl) reference electrode, to sequentially visualize compositional transformations and morphological changes of KI-pretreated hexagonally ordered Cu arrays during CO_2RR.[35] To mitigate electron beam artifacts, the electron flux was controlled to remain below 3.5 $e^- Å^{-2} s^{-1}$. Hexagonally ordered Cu arrays, serving as catalyst precursors, were fabricated using nanosphere lithography and physical vapor deposition techniques. A notable influence of the electrolyte composition on the resulting catalyst morphology was observed, with the hexagonal Cu islands maintaining their structural stability when immersed in Milli-Q pure water under OCP conditions (**Figure 9a**).

Nevertheless, upon replacing pure water with a 0.01 M KI aqueous solution, a progressive reduction in the size of the Cu islands was observed, accompanied by the emergence of small and fragmented particles surrounding the Cu islands, even in the absence of applied cathodic bias (**Figure 9b**). The distinctive peak corresponding to the oxidation of Cu^0 to Cu^+ was discerned following anodic cyclic voltammetry (CV) treatment (between OCP and 0.60 V vs. RHE), indicating that the initial components

transformed during the anodizing process, resulting in the formation of relatively stable CuI species. Following the anodic oxidation of Cu islands in aqueous KI solution, continuous delivery of fresh CO_2-saturated 0.1 M $KHCO_3$ solution and the application of negative bias were employed to observe the morphological evolution of CuI species during CO_2 electrolysis (**Figure 9c**). As shown in **Figures 9d-e**, the CuI nanoparticles remained stable during the first 30 s of the reaction process with an applied potential of −1 V vs. RHE. After 35 s, significant chemical and structural alterations occurred, leading to the transformation of CuI NPs into fragmented filaments (**Figures 9f-g**). The emergence of a reduction peak in the LSV curve indicates that the Cu^+, formed after anodic oxidation, was reduced to Cu^0.

Interestingly, in addition to *in situ* morphological reconstruction during the CO_2RR process, secondary reconstruction of the catalyst was detected following the removal of biasing voltage. Upon discontinuation of the potential, the Cu filament network underwent aggregation and oxidation under OCP, resulting in the formation of a reconstructed tetrahedral configuration within the field of view at 145 s (**Figures 9h-k**). *Ex situ* SAED and EDX mapping confirmed that the restructured compositions comprised a mixture of Cu_2O and CuI, with the tetrahedral structures specifically identified as CuI. In this work, the occurrence of redox processes between Cu^0 and Cu^+ was inferred from the appearance of oxidation and reduction peaks in LSV and CV curves. However, this strategy may be constrained by the complex composition of the electrocatalyst, making it challenging to ascertain changes in the valence state of the target element when multiple redox processes occur simultaneously or sequentially at the electrode. Additionally, the LSV and CV scans differ from actual CO_2 electrolysis operating conditions, potentially affecting the catalyst's morphology. Therefore, we advocate the use of *in situ* TEM coupled with EELS to achieve real-time identification of the valence states of target elements in catalysts.[175-178]

Beyond Cu-based catalysts, bismuth (Bi)-based metal electrocatalysts have been demonstrated to

enhance formic acid (HCOOH) selectivity and mitigate the HER in CO_2RR.[179-182] While some studies have explored the morphological and chemical composition changes of Bi-based catalysts before and after CO_2RR, as well as proposed electrochemical transformation mechanisms, a comprehensive understanding of the dynamics of crystal structure and composition requires further elucidation through *in situ* characterization methods.[183,184] Recently, B. Ávila-Bolívar et al. employed *in situ* LC-TEM strategy to unveil the transformation mechanisms underlying the electrochemical reductive reconfiguration of Bi_2O_3 nanoparticles into Bi nanosheets during CO_2 electrolysis.[38] Initially, the impact of a flowing 0.1 M $KHCO_3$ electrolyte on the structural alterations of carbon-loaded Bi_2O_3 nanoparticles was examined (**Figure 10a**). During the initial 3 minutes of electrolyte solution delivery at OCP, Bi_2O_3 retained a sheet-like structure of approximately 200 nm, with instances of Bi_2O_3 agglomeration into spherical structures. Between 3 and 5 minutes, the bright nanosheets in the field of view underwent extensive reorganization, moving and interconnecting to form larger star-shaped networks ranging from 400 to 700 nm.

After 5 min, these structures ceased further changes in shape or size. Subsequently, the impact of various potentials on the alterations of the Bi-based stellar structure under CO_2 electrolysis conditions was explored using *in situ* LC-TEM. The evolution of the Bi-based stellar structure was continuously monitored via chronoamperometry for up to 1 hour at different applied potentials (−0.3, −0.4, and −0.5 V vs. RHE) (**Figures 10b-g**). Operando Raman findings suggested that at potentials below −0.3 V vs. RHE, Bi-based oxides underwent electrochemical reduction to metallic Bi. Analysis of the data from *in situ* LC-TEM at various potentials indicated that the stellar network comprising Bi_2O_3 remained unaltered at a less negative potential (−0.3 V vs. RHE) (**Figures 10b-c**). However, as shown in **Figures 10d-g**, with the application of more negative potentials (−0.4 and −0.5 V vs. RHE), the stability of the crystal structure is progressively challenged, exhibiting phenomena such as crystal structure changes and lattice oxygen mobility.

Moreover, the mechanism of transformation of Bi_2O_3 particles into Bi nanosheets during CO_2 electrolysis has also been explored through *ex situ* characterizations by Lee et al.[184] They suggested that applying potential induces morphological transformation of Bi_2O_3 particle, and that Bi nanosheets arise from the removal of lattice oxygen from the surface of Bi_2O_3 particles. In contrast, *in situ* TEM experiments from Ávila-Bolívar et al. demonstrated the occurrence of pre-reconstruction of Bi_2O_3 particles without applied potential, likely due to the intrinsic properties of Bi-based materials. This phenomenon underscores the differences between *ex situ* and *in situ* characterization techniques in CO_2RR studies, leading to differing conclusions.

4. Challenges of *in situ* LC-TEM for electrochemical CO_2RR

The primary challenge in employing *in situ* liquid cell STEM/TEM techniques for time-resolved studies of CO_2 electrolysis lies in achieving high spatial resolution and maintaining the credibility of imaging samples in liquid media. To enhance the resolution of *in situ* TEM imaging, we primarily considered the effects related to the liquid electrolyte and the side effects induced by the electron beam. Additionally, the reliability and accuracy of *in situ* studies depend on standardized electrochemical measurement methods and the appropriate selection of electrodes during CO_2 electrolysis in liquid cells. Therefore, we will next discuss the challenges associated with *in situ* LC-TEM, focusing on spatial resolution and electrochemical measurements.

4.1 Spatial resolution

As previously noted, common *in situ* LC-TEM testing is achieved by encapsulating the liquid between two SiN_x electron transparent windows, with the entire assembly consisting commonly of an approximately 300 nm liquid layer and a 100 nm SiN_x window. Liquid thickness is a critical parameter affecting TEM imaging resolution, as thicker liquid layers limit this resolution.[28-38] The liquid layer thickness can also change slightly during electrocatalysis experiments.[185,186] Variations in liquid layer thickness are primarily attributed to the vacuum environment of the TEM column and the applied

external biasing. First, the SiN_x window used to seal the liquid will expand under the pressure difference between the high vacuum (outside) and the near ambient pressure (inside the cell). This expansion leads to an increase in the liquid layer thickness, reducing spatial resolution due to beam spreading and chromatic aberration, the extent of which depends on the mechanical properties of the SiN_x.[187] The gap between the windows determines the liquid thickness, including the thickness of the gasket and the displacement caused by window bulging. Additionally, electrowetting and electric field distribution due to the applied bias can also impact the sealed electrolyte .[186] To estimate the thickness of the liquid layer in the sample chamber when the liquid medium fills the chamber, the relative thickness can be measured using the EELS test.[188,189] According to Lambert-Beer law, $t/\lambda = -\ln(I_0/I_t)$, the relative thickness is determined by the ratio of the number of zero-loss electrons (I_0) to the total number of incident electrons (I_t) in the EELS spectrum. The overall relative thickness consists of two components: the relative thickness of the dry cell and the relative thickness of the liquid. By subtracting the relative thickness of the dry cell, the actual liquid thickness (t_{liquid}) can be expressed by the following formula[189]:

$$t_{liquid} = \left[\left(\frac{t}{\lambda}\right)_{overall} - \left(\frac{t}{\lambda}\right)_{dry\ cell}\right]\lambda_{liquid}$$

Where t is the respective thickness and λ is the inelastic mean free path of the electrons.

To reduce the thickness of the liquid layer, the "Stop and Go" strategy can be employed during CO_2 electrolysis, wherein the potential is halted, and most of the electrolyte is removed. Additionally, the relative thickness of the liquid layer can be estimated using the valence electron EELS test.

The electron beam, with energy greater than 10 eV (the valence electron bonding energy of water), impinging the liquid layer can induce water radiolysis, producing hydrated electrons (e_h^-), hydrogen radicals $H^\bullet$, hydroxyl radicals $OH^\bullet$, and H_2.[190-192] Lee et al. utilized time-resolved liquid cell EELS to identify several molecular products (CO_2, CO, O_2, H_2O_2, and H_2) that result from the interaction of the electron beam with aqueous carbonate solutions.[193]

Moreover, high electron dose rates may lead to undesirable effects such as catalyst degradation and changes in OCP.[186,194] These effects are detrimental to *in situ* observations of CO_2 electrolysis. Therefore, two main solution strategies are recommended: the application of low electron dose rates and the introduction of non-reactive additives into the solution under observation. Generally, a low electron dose rate of 10-20 e^- nm^{-2} s^{-1} is applied during *in situ* LC-TEM experiments to avoid electron beam-induced artefacts.[28-38] Controlled experiments must be conducted to determine the limit of the electron dose rate to ensure that electron beam irradiation does not affect the experiment. Furthermore, studies have shown that adding additives such as ethanol and isopropanol to electrolytes can mitigate adverse irradiation damage to materials examined in liquids.[195,196] The catalyst particle size should not be too large, as this could result in imperfect sealing of the two electron-transparent windows. Sealing issues can cause the electrolyte to evaporate, leading to a decrease in vacuum and spatial resolution of the TEM column.[190] In addition to careful cell assembly, liquid phase media with lower vapor pressure (e.g. glycerol) can be used to buffer or reduce the vapor pressure, thereby reducing the volatility of the liquid in the sample chamber without affecting the CO_2 electrolysis process.[197]

4.2 Electrochemical measurements

The validity of *in situ* CO_2 electrolysis studies relies on the precise and reliable implementation of electrochemical testing methodologies, as well as the accurate control of the electrochemical potential at the working electrode.[198,199] Consequently, the availability of suitable electrochemical measurements and reference electrodes (REs) within cells is imperative for conducting rigorous *in situ* visualization of CO_2 electrolysis.[200-204] As discussed in Section 2, the catalyst structure undergoes various dynamic changes under different electrochemical testing methods (such as LSV, CV and pulsed electrolysis) and applied potentials. For instance, OCP is the equilibrium potential relative to a RE. The known OCP value facilitates setting the potential scanning range for subsequent CO_2 electrolysis.[205-208] Therefore, researchers typically need to verify through controlled experiments whether the

application of OCP and LSV scanning (from OCP to the applied potential) affects the target catalyst's morphology. Moreover, different gradients of cathodic potential are often set to observe diverse morphological changes within the potential scanning range.[35] Correlating the applied electrochemical potentials with the microstructural response of the electrocatalysts aids in elucidating activation and deactivation mechanisms.

In electrochemical experiments, for a specific reaction to proceed in a liquid cell, a stable potential must be externally applied to the working electrode.[122,199] Ensuring the reproducibility and accuracy of CO_2 electrolysis experiments necessitates precise potential control. Therefore, a RE is required as a potential reference standard to provide stable potentials, facilitate potential measurement, and ensure experimental reliability. While the sub-micron size of liquid cells poses challenges for accommodating standard REs (e.g., Ag/AgCl in 3M KCl) and forming salt bridges, some examples of this setup do exist.[35,38] Consequently, many studies have employed platinum, which is chemically stable, has a wide potential window, and is easily nanofabricated, as the pseudoreference electrode.[28-34,36,37] For the accuracy, comparability, and validity of electrocatalytic experiments, both conventional and quasi- or pseudo-REs must possess two properties: a known (standard) electrochemical potential and the ability to remain undisturbed throughout the electrocatalytic experiments, maintaining constant and accurate electrochemical potentials without drift.[209] To achieve accurate electrochemical potentials in *in situ* LC-TEM experiments, Chen et al. calibrated potentials (vs. RHE) for different electrolysis times by applying a linear fit to the change in OCP relative to the Pt pseudoreference electrode over a 200 s period.[30]

During electrochemical CO_2RR processes, gaseous products such as CO and H_2 are inevitably produced, and bubbles can become trapped in the flowing liquid, complicating their removal. These bubbles affect the electrochemical potential of nearby REs and cause irregular flow of the electrolyte solution in the cell observation area, leading to an unstable CO_2 electrolysis and imaging processes. Additionally,

bubbles deactivate catalyst particles by displacing the electrolyte solution, effectively halting the reaction. Under these conditions, experiments must be designed to minimize bubble formation. Beyond reducing catalyst loading and adjusting the applied potential, managing electrolyte flow can help mitigate bubble formation issues in the liquid cell. Increasing the hydrophilicity of the top and bottom windows through plasma cleaning is another strategy to achieve more controlled liquid flow and easier bubble detachment from inner cell surfaces. Moreover, Garza et al. demonstrated a strategy to modulate bubble dissolution via pressure control.[210] Gas bubbles are generated by splitting water on the surface of the working electrode. By varying the internal pressure of the liquid cell, the dissolution of gas back into the liquid can be controlled.

5. Conclusions and outlook

In situ LC-TEM studies offer valuable insights into electrochemical CO_2RR. By examining how electrocatalysts evolve over time and correlating these changes with the distribution of CO_2RR products, we can identify the active components and establish clear structure-activity relationships. Moreover, by integrating control over applied potential with monitoring the evolution of catalyst morphology, researchers can elucidate the reaction mechanisms underlying catalyst activation and deactivation. These approaches significantly enhance our comprehension of the electrochemical CO_2RR mechanisms, thereby facilitating the development of high-performance electrocatalysts.

This review begins with an introduction to *in situ* LC-TEM, tracing its evolution. Following this, we explore its application in CO_2 electrolysis. We review the extant body of *in situ* LC-TEM studies that visualize CO_2 electrolysis, discussing dynamic morphological evolution, size effects, the identification of active sites, and the transformation of crystal structures and compositions. This review also highlights the advantages, limitations, and complementarities of current TEM imaging techniques, addressing the challenges of achieving high-resolution and high-reliability *in situ* LC-TEM imaging. Based on existing studies, we propose coupling *in situ* LC-TEM with SAED or 4D STEM for crystal

structure analysis, EELS for valence state analysis, and EDX for elemental distribution analysis. Additionally, we discuss the challenges associated with time-resolved visualization of CO_2RR, particularly concerning spatial resolution and electrochemical measurements, and provide suggestions to address these issues. Despite the nascent nature of current *in situ* LC-TEM methodologies for investigating CO_2 electrolysis, achieving a thorough and profound understanding of the dynamic CO_2RR processes remains challenging. Within this review, we outline the following recommendations for advancing *in situ* LC-TEM studies in the realm of CO_2 electrolysis:

1. Refinement of chip fabrication: The typical liquid cell thickness for *in situ* electrochemical LC-STEM/TEM, often exceeding 300 nm, poses challenges in resolving structural details for nanoparticles smaller than 10 nm. Beyond the intrinsic thickness of the liquid cell, considerations must also be given to the increased thickness of the liquid layer caused by the bulging of SiNx film. Wu et al. observed inward bulging of SiNx thin films by modulating the internal pressure of the cell, thus creating an ultra-thin liquid layer in the central window area conducive for high-resolution imaging.[211] Additionally, operational conditions cause the liquid to flow along the chip's edge, leading to notably higher relative velocities at the periphery than at the central region.[212] Consequently, optimizing chip geometry, such as designing anti-swelling chips[213], utilizing ultra-thin SiN_x[214] or polymer films[68], and employing liquid-flowing graphene chips[215] and monolithic chips[216] can effectively minimize liquid layer thickness, thus facilitating robust high-resolution imaging without bulging while ensuring stable mass transport and improved microfluidic properties for CO_2 electrolysis. Given that electrocatalyst stability is a constraint in industrial applications, long-term degradation studies will necessitate chips that maintain high stability throughout the process. However, the potential breakage of the SiNx film after prolonged experimental use may undermine the chip's stability and reliability. Monolithic chips with microfluidic channels across a suspended electron-transparent membrane can effectively resolve these issues and improve *in situ* observation stability, along with addressing alignment and sealing challenges during cell assembly.[216]

2. Development of advanced imaging technologies: The spatial and temporal resolution in liquid samples is typically constrained by the maximum allowable beam dose. The energy emitted by the electron excitation source In TEM experiments can be excessively strong for certain structurally delicate electrocatalysts, such as bismuth-based materials.[217] Advanced imaging techniques have been devised to mitigate this issue. For instance, 4D-STEM, can nowadays be obtained in modern hybrid detectors, which are known for their single-electron sensitivity, extensive dynamic range, and rapid readout speed of up to 10,000 frames per second. Consequently, this technique is well-suited for conducting low-dose electron diffraction of beam-sensitive samples in liquid environments.[154,218] In vacuum conditions, 4D-STEM diffraction imaging has achieved sub-angstrom real-space resolution and sub-picometer reciprocal-space resolution.[219] In liquid settings, it provides nanometer-scale real-space resolution and sub-angstrom reciprocal-space resolution, thereby offering valuable structural insights.[34,220]

3. Integration of machine learning: To tackle challenges in TEM image analysis, researchers have endeavored to integrate automated methodologies with image processing techniques.[221,222] Machine learning, in particular, has emerged as a promising avenue for automating TEM image analysis, including tasks such as defect identification[223], morphology assessment[224], structure analysis[225,226], and spectra characterization[227] of nanomaterials. As *in situ* TEM techniques advance in both temporal and spatial resolution, the large volume of data generated within short timeframes presents significant hurdles for data transfer and storage. Recent studies have demonstrated that efficient compression of vast amounts of electron microscopy data can be realized through deep compression-aware learning methodologies, providing a promising strategy for processing long-term *in situ* TEM images.[228]

References

1. Gattuso, J.P., Magnan, A., Billé, R., et al. (2015). Contrasting futures for ocean and society from different anthropogenic CO_2 emissions scenarios. Science **349**(6243):aac4722. https://doi.org/10.1126/science.aac4722.

2. Wang, Y., Wang, Z., Dinh, C.-T., et al. (2020). Catalyst synthesis under CO_2 electroreduction favours faceting and promotes renewable fuels electrosynthesis. Nature Catalysis **3**(2):98-106. https://doi.org/10.1038/s41929-019-0397-1.

3. Zhang, S., Fan, Q., Xia, R., and Meyer, T.J. (2020). CO_2 reduction: From homogeneous to heterogeneous electrocatalysis. Accounts of Chemical Research **53**(1):255-264. https://doi.org/10.1021/acs.accounts.9b00496.

4. Wu, J., Huang, Y., Ye, W., and Li, Y. (2017). CO_2 reduction: From the electrochemical to photochemical approach. Advanced Science **4**(11):1700194. https://doi.org/10.1002/advs.201700194.

5. Wang, X., Ou, P., Wicks, J., et al. (2021). Gold-in-copper at low $^{*}CO$ coverage enables efficient electromethanation of CO_2. Nature Communications **12**(1):3387. https://doi.org/10.1038/s41467-021-23699-4.

6. Ren, D., Fong, J., and Yeo, B.S. (2018). The effects of currents and potentials on the selectivities of copper toward carbon dioxide electroreduction. Nature Communications **9**(1):925. https://doi.org/10.1038/s41467-018-03286-w.

7. Wang, X., Xu, A., Li, F., et al. (2020). Efficient methane electrosynthesis enabled by tuning local CO_2 availability. Journal of the American Chemical Society **142**(7):3525-3531. https://doi.org/10.1021/jacs.9b12445.

8. Chen, Y., Li, X.-Y., Chen, Z., et al. (2024). Efficient multicarbon formation in acidic CO_2 reduction via tandem electrocatalysis. Nature Nanotechnology **19**(3):311-318. https://doi.org/10.1038/s41565-023-01543-8.

9. Huang, J.E., Li, F., Ozden, A., et al. (2021). CO_2 electrolysis to multicarbon products in strong acid. Science **372**(6546):1074-1078. https://doi.org/10.1126/science.abg6582.

10. Xie, Y., Ou, P., Wang, X., et al. (2022). High carbon utilization in CO_2 reduction to multi-carbon products in acidic media. Nature Catalysis **5**(6):564-570. https://doi.org/10.1038/s41929-022-00788-1.

11. Fan, M., Huang, J.E., Miao, R.K., et al. (2023). Cationic-group-functionalized electrocatalysts enable stable acidic CO_2 electrolysis. Nature Catalysis **6**(9):763-772. https://doi.org/10.1038/s41929-023-01003-5.

12. Crandall, B.S., Ko, B.H., Overa, S., et al. (2024). Kilowatt-scale tandem CO_2 electrolysis for enhanced acetate and ethylene production. Nature Chemical Engineering **1**(6):421-429. https://doi.org/10.1038/s44286-024-00076-8.

13. Wang, H., Kang, X., and Han, B. (2024). Rare-earth element-based electrocatalysts designed for CO_2 electro-reduction. ChemSusChem **17**(7):e202301539. https://doi.org/10.1002/cssc.202301539.

14. Liu, J., Li, P., Bi, J., et al. (2023). Switching between C_{2+} products and CH_4 in CO_2 electrolysis by tuning the composition and structure of rare-earth/copper catalysts. Journal of the American Chemical Society **145**(42):23037-23047. https://doi.org/10.1021/jacs.3c05562.

15. Feng, J., Wu, L., Liu, S., et al. (2023). Improving CO_2-to-C_{2+} product electroreduction efficiency via atomic lanthanide dopant-induced tensile-strained CuOx catalysts. Journal of the American Chemical Society **145**(17):9857-9866. https://doi.org/10.1021/jacs.3c02428.

16. Feng, J., Wu, L., Song, X., et al. (2024). CO_2 electrolysis to multi-carbon products in strong acid at ampere-current levels on La-Cu spheres with channels. Nature Communications **15**(1):4821. https://doi.org/10.1038/s41467-024-49308-8.

17. Lum, Y., Cheng, T., Goddard, W.A., III, and Ager, J.W. (2018). Electrochemical CO reduction builds solvent water into oxygenate products. Journal of the American Chemical Society **140**(30):9337-9340.

https://doi.org/10.1021/jacs.8b03986.

18. Nitopi, S., Bertheussen, E., Scott, S.B., et al. (2019). Progress and perspectives of electrochemical CO_2 reduction on copper in aqueous electrolyte. Chemical Reviews **119**(12):7610-7672. https://doi.org/10.1021/acs.chemrev.8b00705.

19. Todorova, T.K., Schreiber, M.W., and Fontecave, M. (2020). Mechanistic understanding of CO_2 reduction reaction (CO_2RR) toward multicarbon products by heterogeneous copper-based catalysts. ACS Catalysis **10**(3):1754-1768. https://doi.org/10.1021/acscatal.9b04746.

20. Kortlever, R., Shen, J., Schouten, K.J.P., et al. (2015). Catalysts and reaction pathways for the electrochemical reduction of carbon dioxide. The Journal of Physical Chemistry Letters **6**(20):4073-4082. https://doi.org/10.1021/acs.jpclett.5b01559.

21. Schouten, K.J.P., Kwon, Y., van der Ham, C.J.M., et al. (2011). A new mechanism for the selectivity to C_1 and C_2 species in the electrochemical reduction of carbon dioxide on copper electrodes. Chemical Science **2**(10):1902-1909. https://doi.org/10.1039/C1SC00277E.

22. Garza, A.J., Bell, A.T., and Head-Gordon, M. (2018). Mechanism of CO_2 reduction at copper surfaces: Pathways to C_2 products. ACS Catalysis **8**(2):1490-1499. https://doi.org/10.1021/acscatal.7b03477.

23. Su, X., Jiang, Z., Zhou, J., et al. (2022). Complementary Operando Spectroscopy identification of in-situ generated metastable charge-asymmetry Cu_2-CuN_3 clusters for CO_2 reduction to ethanol. Nature Communications **13**(1):1322. https://doi.org/10.1038/s41467-022-29035-8.

24. Handoko, A.D., Wei, F., Jenndy, et al. (2018). Understanding heterogeneous electrocatalytic carbon dioxide reduction through operando techniques. Nature Catalysis **1**(12):922-934. https://doi.org/10.1038/s41929-018-0182-6.

25. Gao, D., Arán-Ais, R.M., Jeon, H.S., and Roldan Cuenya, B. (2019). Rational catalyst and electrolyte design for CO_2 electroreduction towards multicarbon products. Nature Catalysis **2**(3):198-210. https://doi.org/10.1038/s41929-019-0235-5.

26. Wagner, A., Sahm, C.D., and Reisner, E. (2020). Towards molecular understanding of local chemical environment effects in electro- and photocatalytic CO_2 reduction. Nature Catalysis **3**(10):775-786. https://doi.org/10.1038/s41929-020-00512-x.

27. Wang, J., Hsu, C.-S., Wu, T.-S., et al. (2023). In situ X-ray spectroscopies beyond conventional X-ray absorption spectroscopy on deciphering dynamic configuration of electrocatalysts. Nature Communications **14**(1):6576. https://doi.org/10.1038/s41467-023-42370-8.

28. Li, Y., Kim, D., Louisia, S., et al. (2020). Electrochemically scrambled nanocrystals are catalytically active for CO_2-to-multicarbons. Proceedings of the National Academy of Sciences **117**(17):9194-9201. https://doi.org/10.1073/pnas.1918602117.

29. Wang, X., Klingan, K., Klingenhof, M., et al. (2021). Morphology and mechanism of highly selective Cu(II) oxide nanosheet catalysts for carbon dioxide electroreduction. Nature Communications **12**(1):794. https://doi.org/10.1038/s41467-021-20961-7.

30. Hsu, C.-S., Wang, J., Chu, Y.-C., et al. (2023). Activating dynamic atomic-configuration for single-site electrocatalyst in electrochemical CO_2 reduction. Nature Communications **14**(1):5245. https://doi.org/10.1038/s41467-023-40970-y.

31. Grosse, P., Yoon, A., Rettenmaier, C., et al. (2021). Dynamic transformation of cubic copper catalysts during CO_2 electroreduction and its impact on catalytic selectivity. Nature Communications **12**(1):6736. https://doi.org/10.1038/s41467-021-26743-5.

32. Arán-Ais, R.M., Rizo, R., Grosse, P., et al. (2020). Imaging electrochemically synthesized Cu_2O cubes and their morphological evolution under conditions relevant to CO_2 electroreduction. Nature Communications **11**(1):3489. https://doi.org/10.1038/s41467-020-17220-6.

33. Abdellah, A.M., Ismail, F., Siig, O.W., et al. (2024). Impact of palladium/palladium hydride conversion on electrochemical CO_2 reduction via in-situ transmission electron microscopy and diffraction. Nature Communications **15**(1):938. https://doi.org/10.1038/s41467-024-45096-3.

34. Yang, Y., Louisia, S., Yu, S., et al. (2023). Operando studies reveal active Cu nanograins for CO_2 electroreduction. Nature **614**(7947):262-269. https://doi.org/10.1038/s41586-022-05540-0.

35. Yoon, A., Poon, J., Grosse, P., et al. (2022). Iodide-mediated Cu catalyst arestructuring during CO_2 electroreduction. Journal of Materials Chemistry A **10**(26):14041-14050. https://doi.org/10.1039/D1TA11089F.

36. Vavra, J., Shen, T.-H., Stoian, D., et al. (2021). Real-time monitoring reveals dissolution/redeposition mechanism in copper nanocatalysts during the initial stages of the CO_2 reduction reaction. Angewandte Chemie International Edition **60**(3):1347-1354. https://doi.org/10.1002/anie.202011137.

37. Yang, Y., Shao, Y.-T., Jin, J., et al. (2023). Operando electrochemical liquid-cell scanning transmission electron microscopy (EC-STEM) studies of evolving Cu nanocatalysts for CO_2 electroreduction. ACS Sustainable Chemistry & Engineering **11**(10):4119-4124. https://doi.org/10.1021/acssuschemeng.2c06542.

38. Ávila-Bolívar, B., Lopez Luna, M., Yang, F., et al. (2024). Revealing the intrinsic restructuring of Bi_2O_3 nanoparticles into Bi nanosheets during electrochemical CO_2 reduction. ACS Applied Materials & Interfaces **16**(9):11552-11560. https://doi.org/10.1021/acsami.3c18285.

39. Mayrhofer, K.J.J., Ashton, S.J., Meier, J.C., et al. (2008). Non-destructive transmission electron microscopy study of catalyst degradation under electrochemical treatment. Journal of Power Sources **185**(2):734-739. https://doi.org/10.1016/j.jpowsour.2008.08.003.

40. Pelaez-Fernandez, M., Bermejo, A., Benito, A.M., et al. (2021). Detailed thermal reduction analyses of graphene oxide via in-situ TEM/EELS studies. Carbon **178**:477-487. https://doi.org/10.1016/j.carbon.2021.03.018.

41. Cui, J., Zheng, H., and He, K. (2021). In situ TEM study on conversion-type electrodes for rechargeable ion batteries. Advanced Materials **33**(6):2000699. https://doi.org/10.1002/adma.202000699.

42. Zhang, Y., Gore, P., Rong, W., et al. (2018). Quasi-in-situ STEM-EDS insight into the role of Ag in the corrosion behaviour of Mg-Gd-Zr alloys. Corrosion Science **136**:106-118. https://doi.org/10.1016/j.corsci.2018.02.058.

43. Lambert, L., and Mulvey, T. (1996). Ernst Ruska (1906–1988), Designer Extraordinaire of the Electron Microscope: A Memoir. In Advances in Imaging and Electron Physics, P.W. Hawkes, ed. (Elsevier), pp. 2-62. https://doi.org/10.1016/S1076-5670(08)70155-1.

44. Ruska, E. (1987). The development of the electron microscope and of electron microscopy (Nobel lecture). Angewandte Chemie International Edition in English **26**(7):595-605. https://doi.org/10.1002/anie.198705953.

45. Ruska, E. (1987). The development of the electron microscope and of electron microscopy. Reviews of Modern Physics **59**(3):627-638. https://doi.org/10.1103/RevModPhys.59.627.

46. Egerton, R.F. (2009). Electron energy-loss spectroscopy in the TEM. Reports on Progress in Physics **72**(1):016502. https://doi.org/10.1088/0034-4885/72/1/016502.

47. Poppa, H. (1965). Progress in the continuous observation of thin-film nucleation and growth processes by electron microscopy. Journal of Vacuum Science and Technology **2**(1):42-48. https://doi.org/10.1116/1.1492397.

48. Liao, H.-G., and Zheng, H. (2016). Liquid cell transmission electron microscopy. Annual Review of Physical Chemistry **67**(Volume 67, 2016):719-747. https://doi.org/10.1146/annurev-physchem-040215-112501.

49. Pu, S., Gong, C., and Robertson, A.W. (2020). Liquid cell transmission electron microscopy and its applications. Royal Society Open Science **7**(1):191204. https://doi.org/10.1098/rsos.191204.

50. Nielsen, M.H., Li, D., Zhang, H., et al. (2014). Investigating processes of nanocrystal formation and transformation via liquid cell TEM. Microscopy and Microanalysis **20**(2):425-436. https://doi.org/10.1017/S1431927614000294.

51. Parent, L.R., Bakalis, E., Proetto, M., et al. (2018). Tackling the challenges of dynamic experiments using liquid-cell transmission electron microscopy. Accounts of Chemical Research **51**(1):3-11. https://doi.org/10.1021/acs.accounts.7b00331.

52. Ross, F.M. (2015). Opportunities and challenges in liquid cell electron microscopy. Science **350**(6267):aaa9886. https://doi.org/10.1126/science.aaa9886.

53. Parsons, D.F. (1974). Structure of wet specimens in electron microscopy. Science **186**(4162):407-414. https://doi.org/10.1126/science.186.4162.407.

54. Williamson, M.J., Tromp, R.M., Vereecken, P.M., et al. (2003). Dynamic microscopy of nanoscale cluster growth at the solid–liquid interface. Nature Materials **2**(8):532-536. https://doi.org/10.1038/nmat944.

55. Zheng, H., Smith, R.K., Jun, Y.-w., et al. (2009). Observation of single colloidal platinum nanocrystal growth trajectories. Science **324**(5932):1309-1312. https://doi.org/10.1126/science.1172104.

56. Yuk, J.M., Park, J., Ercius, P., et al. (2012). High-resolution EM of colloidal nanocrystal growth using graphene liquid cells. Science **336**(6077):61-64. https://doi.org/10.1126/science.1217654.

57. Park, J., Park, H., Ercius, P., et al. (2015). Direct observation of wet biological samples by graphene liquid cell transmission electron microscopy. Nano Letters **15**(7):4737-4744. https://doi.org/10.1021/acs.nanolett.5b01636.

58. Textor, M., and de Jonge, N. (2018). Strategies for preparing graphene liquid cells for transmission electron microscopy. Nano Letters **18**(6):3313-3321. https://doi.org/10.1021/acs.nanolett.8b01366.

59. Park, J., Koo, K., Noh, N., et al. (2021). Graphene liquid cell electron microscopy: Progress, applications, and perspectives. ACS Nano **15**(1):288-308. https://doi.org/10.1021/acsnano.0c10229.

60. Kelly, D.J., Zhou, M., Clark, N., et al. (2018). Nanometer resolution elemental mapping in graphene-based TEM liquid cells. Nano Letters **18**(2):1168-1174. https://doi.org/10.1021/acs.nanolett.7b04713.

61. Yang, R., Mei, L., Fan, Y., et al. (2023). Fabrication of liquid cell for in situ transmission electron microscopy of electrochemical processes. Nature Protocols **18**(2):555-578. https://doi.org/10.1038/s41596-022-00762-y.

62. Chee, S.W., Tan, S.F., Baraissov, Z., et al. (2017). Direct observation of the nanoscale Kirkendall effect during galvanic replacement reactions. Nature Communications **8**(1):1224. https://doi.org/10.1038/s41467-017-01175-2.

63. Wu, J., Shan, H., Chen, W., et al. (2016). In situ environmental TEM in imaging gas and liquid phase chemical reactions for materials research. Advanced Materials **28**(44):9686-9712. https://doi.org/10.1002/adma.201602519.

64. He, B., Zhang, Y., Liu, X., and Chen, L. (2020). In-situ transmission electron microscope techniques for heterogeneous catalysis. ChemCatChem **12**(7):1853-1872. https://doi.org/10.1002/cctc.201902285.

65. Tsoukalou, A., Abdala, P.M., Stoian, D., et al. (2019). Structural evolution and dynamics of an In_2O_3 catalyst for CO_2 hydrogenation to methanol: An operando XAS-XRD and in situ TEM study. Journal of the American Chemical Society **141**(34):13497-13505. https://doi.org/10.1021/jacs.9b04873.

66. Xiao, L., Wang, G., Huang, X., et al. (2022). Efficient CO_2 reduction MOFs derivatives transformation mechanism revealed by in-situ liquid phase TEM. Applied Catalysis B: Environment and Energy **307**:121164. https://doi.org/10.1016/j.apcatb.2022.121164.

67. Su, L., Ren, J., Lu, T., et al. (2023). Deciphering structural origins of highly reversible lithium storage in high entropy oxides with in situ transmission electron microscopy. Advanced Materials **35**(19):2205751. https://doi.org/10.1002/adma.202205751.

68. Zhang, Q., Song, Z., Sun, X., et al. (2024). Atomic dynamics of electrified solid–liquid interfaces in liquid-cell TEM. Nature **630**(8017):643-647. https://doi.org/10.1038/s41586-024-07479-w.

69. Braidy, N., Béchu, A., de Souza Terra, J.C., and Patience, G.S. (2020). Experimental methods in chemical engineering: Transmission electron microscopy—TEM. The Canadian Journal of Chemical Engineering **98**(3):628-641. https://doi.org/10.1002/cjce.23692.

70. Brydson, R., Brown, A., Benning, L.G., and Livi, K. (2014). Analytical transmission electron microscopy. Reviews in Mineralogy and Geochemistry **78**(1):219-269. https://doi.org/10.2138/rmg.2014.78.6.

71. de Jonge, N., and Ross, F.M. (2011). Electron microscopy of specimens in liquid. Nature Nanotechnology **6**(11):695-704. https://doi.org/10.1038/nnano.2011.161.

72. Foucher, A.C., and Stach, E.A. (2023). High Pressure Transmission Electron Microscopy (TEM). In Springer Handbook of Advanced Catalyst Characterization, I.E. Wachs, and M.A. Bañares, eds. (Springer International Publishing), pp. 381-407. https://doi.org/10.1007/978-3-031-07125-6_19.

73. Taheri, M.L., Stach, E.A., Arslan, I., et al. (2016). Current status and future directions for in situ transmission electron microscopy. Ultramicroscopy **170**:86-95. https://doi.org/10.1016/j.ultramic.2016.08.007.

74. Tromp, R.M., and Ross, F.M. (2000). Advances in in situ ultra-high vacuum electron microscopy: Growth of SiGe on Si. Annual Review of Materials Research **30**(Volume 30, 2000):431-449. https://doi.org/10.1146/annurev.matsci.30.1.431.

75. Howe, J.M., and Saka, H. (2004). In situ transmission electron microscopy studies of the solid–liquid interface. MRS Bulletin **29**(12):951-957. https://doi.org/10.1557/mrs2004.266.

76. Eswaramoorthy, S.K., Howe, J.M., and Muralidharan, G. (2007). In situ determination of the nanoscale chemistry and behavior of solid-liquid systems. Science **318**(5855):1437-1440. https://doi.org/10.1126/science.1146511.

77. Ross, F.M., Tersoff, J., and Reuter, M.C. (2005). Sawtooth faceting in silicon nanowires. Physical Review Letters **95**(14):146104. https://doi.org/10.1103/PhysRevLett.95.146104.

78. Keller, D., Henninen, T.R., and Erni, R. (2020). Atomic mechanisms of gold nanoparticle growth in ionic liquids studied by in situ scanning transmission electron microscopy. Nanoscale **12**(44):22511-22517. https://doi.org/10.1039/D0NR06541B.

79. Miyata, T., and Mizoguchi, T. (2017). Fabrication of thin TEM sample of ionic liquid for high-resolution ELNES measurements. Ultramicroscopy **178**:81-87. https://doi.org/10.1016/j.ultramic.2016.10.009.

80. Gonçalves, W.D.G., Zanatta, M., Simon, N.M., et al. (2019). Efficient electrocatalytic CO_2 reduction driven by ionic liquid buffer-like solutions. ChemSusChem **12**(18):4170-4175. https://doi.org/10.1002/cssc.201901076.

81. Shi, J., Shi, F., Song, N., et al. (2014). A novel electrolysis cell for CO_2 reduction to CO in ionic liquid/organic solvent electrolyte. Journal of Power Sources **259**:50-53. https://doi.org/10.1016/j.jpowsour.2014.02.072.

82. Jin, S., Hao, Z., Zhang, K., et al. (2021). Advances and challenges for the electrochemical reduction of CO_2 to CO: From fundamentals to industrialization. Angewandte Chemie International Edition **60**(38):20627-20648. https://doi.org/10.1002/anie.202101818.

83. Gai, P.L., and Boyes, E.D. (2009). Advances in atomic resolution in situ environmental transmission electron microscopy and 1Å aberration corrected in situ electron microscopy. Microscopy Research and Technique **72**(3):153-164. https://doi.org/10.1002/jemt.20668.

84. Jinschek, J.R. (2014). Advances in the environmental transmission electron microscope (ETEM) for nanoscale in situ studies of gas–solid interactions. Chemical Communications **50**(21):2696-2706. https://doi.org/10.1039/C3CC49092K.

85. Zhao, H., Zhu, Y., Ye, H., et al. (2023). Atomic-scale structure dynamics of nanocrystals revealed by in situ and environmental transmission electron microscopy. Advanced Materials **35**(50):2206911. https://doi.org/10.1002/adma.202206911.

86. Boyes, E.D., and Gai, P.L. (2014). Visualising reacting single atoms under controlled conditions: Advances in atomic resolution in situ Environmental (Scanning) Transmission Electron Microscopy (E(S)TEM). Comptes Rendus Physique **15**(2):200-213. https://doi.org/10.1016/j.crhy.2014.01.002.

87. Hansen, T.W., Wagner, J.B., and Dunin-Borkowski, R.E. (2010). Aberration corrected and

monochromated environmental transmission electron microscopy: Challenges and prospects for materials science. Materials Science and Technology **26**(11):1338-1344. https://doi.org/10.1179/026708310X12756557336355.

88. Liu, Q., Geng, L., Yang, T., et al. (2019). In-situ imaging electrocatalysis in a Na-O_2 battery with Au-coated MnO_2 nanowires air cathode. Energy Storage Materials **19**:48-55. https://doi.org/10.1016/j.ensm.2018.08.026.

89. Luo, L., Liu, B., Song, S., et al. (2017). Revealing the reaction mechanisms of Li–O_2 batteries using environmental transmission electron microscopy. Nature Nanotechnology **12**(6):535-539. https://doi.org/10.1038/nnano.2017.27.

90. Kwak, W.-J., Luo, L., Jung, H.-G., et al. (2018). Revealing the reaction mechanism of Na–O_2 batteries using environmental transmission electron microscopy. ACS Energy Letters **3**(2):393-399. https://doi.org/10.1021/acsenergylett.7b01273.

91. Yousaf, M., Naseer, U., Li, Y., et al. (2021). A mechanistic study of electrode materials for rechargeable batteries beyond lithium ions by in situ transmission electron microscopy. Energy & Environmental Science **14**(5):2670-2707. https://doi.org/10.1039/D0EE03295F.

92. Kamaladasa, R.J., Sharma, A.A., Lai, Y.-T., et al. (2015). In situ TEM imaging of defect dynamics under electrical bias in resistive switching rutile-TiO_2. Microscopy and Microanalysis **21**(1):140-153. https://doi.org/10.1017/S1431927614013555.

93. Jeangros, Q., Duchamp, M., Werner, J., et al. (2016). In situ TEM analysis of organic–inorganic metal-halide perovskite solar cells under electrical bias. Nano Letters **16**(11):7013-7018. https://doi.org/10.1021/acs.nanolett.6b03158.

94. Hwang, S., Chen, X., Zhou, G., and Su, D. (2020). In situ transmission electron microscopy on energy-related catalysis. Advanced Energy Materials **10**(11):1902105. https://doi.org/10.1002/aenm.201902105.

95. Ghodsi, S.M., Megaridis, C.M., Shahbazian-Yassar, R., and Shokuhfar, T. (2019). Advances in graphene-based liquid cell electron microscopy: Working principles, opportunities, and challenges. Small Methods **3**(5):1900026. https://doi.org/10.1002/smtd.201900026.

96. Zeng, X., Zhao, Y., Hu, X., et al. (2021). Rational component and structure design of noble-metal composites for optical and catalytic applications. Small Structures **2**(4):2000138. https://doi.org/10.1002/sstr.202000138.

97. Jouny, M., Luc, W., and Jiao, F. (2018). General techno-economic analysis of CO_2 electrolysis systems. Industrial & Engineering Chemistry Research **57**(6):2165-2177. https://doi.org/10.1021/acs.iecr.7b03514.

98. Shin, H., Hansen, K.U., and Jiao, F. (2021). Techno-economic assessment of low-temperature carbon dioxide electrolysis. Nature Sustainability **4**(10):911-919. https://doi.org/10.1038/s41893-021-00739-x.

99. Lai, W., Qiao, Y., Zhang, J., et al. (2022). Design strategies for markedly enhancing energy efficiency in the electrocatalytic CO_2 reduction reaction. Energy & Environmental Science **15**(9):3603-3629. https://doi.org/10.1039/D2EE00472K.

100. Wu, H., Yu, H., Chow, Y.-L., et al. (2024). Toward durable CO_2 electroreduction with Cu-based catalysts via understanding their deactivation modes. Advanced Materials **n/a**(n/a):2403217. https://doi.org/10.1002/adma.202403217.

101. Ren, S., Lees, E.W., Hunt, C., et al. (2023). Catalyst aggregation matters for immobilized molecular CO_2RR electrocatalysts. Journal of the American Chemical Society **145**(8):4414-4420. https://doi.org/10.1021/jacs.2c08380.

102. Trindell, J.A., Clausmeyer, J., and Crooks, R.M. (2017). Size stability and H_2/CO selectivity for Au nanoparticles during electrocatalytic CO_2 reduction. Journal of the American Chemical Society **139**(45):16161-16167. https://doi.org/10.1021/jacs.7b06775.

103. Li, F., Medvedeva, X.V., Medvedev, J.J., et al. (2021). Interplay of electrochemical and electrical effects induces structural transformations in electrocatalysts. Nature Catalysis **4**(6):479-487. https://doi.org/10.1038/s41929-021-00624-y.

104. Clark, E.L., Hahn, C., Jaramillo, T.F., and Bell, A.T. (2017). Electrochemical CO_2 reduction over compressively strained CuAg surface alloys with enhanced multi-carbon oxygenate selectivity. Journal of the American Chemical Society **139**(44):15848-15857. https://doi.org/10.1021/jacs.7b08607.

105. Albertini, P.P., Newton, M.A., Wang, M., et al. (2024). Hybrid oxide coatings generate stable Cu catalysts for CO_2 electroreduction. Nature Materials **23**(5):680-687. https://doi.org/10.1038/s41563-024-01819-x.

106. Okatenko, V., Loiudice, A., Newton, M.A., et al. (2023). Alloying as a strategy to boost the stability of copper nanocatalysts during the electrochemical CO_2 reduction reaction. Journal of the American Chemical Society **145**(9):5370-5383. https://doi.org/10.1021/jacs.2c13437.

107. Overa, S., Crandall, B.S., Shrimant, B., et al. (2022). Enhancing acetate selectivity by coupling anodic oxidation to carbon monoxide electroreduction. Nature Catalysis **5**(8):738-745. https://doi.org/10.1038/s41929-022-00828-w.

108. He, J., Huang, A., Johnson, N.J.J., et al. (2018). Stabilizing copper for CO_2 reduction in low-grade electrolyte. Inorganic Chemistry **57**(23):14624-14631. https://doi.org/10.1021/acs.inorgchem.8b02311.

109. Li, F., Li, Y.C., Wang, Z., et al. (2020). Cooperative CO_2-to-ethanol conversion via enriched intermediates at molecule–metal catalyst interfaces. Nature Catalysis **3**(1):75-82. https://doi.org/10.1038/s41929-019-0383-7.

110. Van Daele, K., De Mot, B., Pupo, M., et al. (2021). Sn-based electrocatalyst stability: A crucial piece to the puzzle for the electrochemical CO_2 reduction toward formic acid. ACS Energy Letters **6**(12):4317-4327. https://doi.org/10.1021/acsenergylett.1c02049.

111. Bagger, A., Ju, W., Varela, A.S., et al. (2017). Electrochemical CO_2 reduction: A classification problem. ChemPhysChem **18**(22):3266-3273. https://doi.org/10.1002/cphc.201700736.

112. Chang, X., Li, J., Xiong, H., et al. (2022). C–C coupling is unlikely to be the rate-determining step in the formation of C_{2+} products in the copper-catalyzed electrochemical reduction of CO. Angewandte Chemie International Edition **61**(2):e202111167. https://doi.org/10.1002/anie.202111167.

113. Hodnik, N., Dehm, G., and Mayrhofer, K.J.J. (2016). Importance and challenges of electrochemical in situ liquid cell electron microscopy for energy conversion research. Accounts of Chemical Research **49**(9):2015-2022. https://doi.org/10.1021/acs.accounts.6b00330.

114. Jiang, Y., Lim, A.M.H., Yan, H., et al. (2023). Phase segregation in PdCu alloy nanoparticles during CO oxidation reaction at atmospheric pressure. Advanced Science **10**(25):2302663. https://doi.org/10.1002/advs.202302663.

115. Hasa, B., Zhao, Y., and Jiao, F. (2023). In situ/operando characterization techniques of electrochemical CO_2 reduction. Annual Review of Chemical and Biomolecular Engineering **14**(Volume 14, 2023):165-185. https://doi.org/10.1146/annurev-chembioeng-101121-071735.

116. Shen, T.-H., Girod, R., Vavra, J., and Tileli, V. (2023). Considerations of liquid-phase transmission electron microscopy applied to heterogeneous electrocatalysis. Journal of The Electrochemical Society **170**(5):056502. https://doi.org/10.1149/1945-7111/acced4.

117. Xia, T., Wang, Z., and Li, F. (2022). Seeing is believing: In-situ visualising dynamic evolution in CO_2 electrolysis. Current Opinion in Electrochemistry **31**:100846. https://doi.org/10.1016/j.coelec.2021.100846.

118. Song, X., Xu, L., Sun, X., and Han, B. (2023). In situ/operando characterization techniques for electrochemical CO_2 reduction. Science China Chemistry **66**(2):315-323. https://doi.org/10.1007/s11426-021-1463-6.

119. Cao, X., Tan, D., Wulan, B., et al. (2021). In situ characterization for boosting electrocatalytic carbon

dioxide reduction. Small Methods **5**(10):2100700. https://doi.org/10.1002/smtd.202100700.

120. Tomboc, G.M., Choi, S., Kwon, T., et al. (2020). Potential link between Cu surface and selective CO_2 electroreduction: Perspective on future electrocatalyst designs. Advanced Materials **32**(17):1908398. https://doi.org/10.1002/adma.201908398.
121. Raciti, D., and Wang, C. (2018). Recent advances in CO_2 reduction electrocatalysis on copper. ACS Energy Letters **3**(7):1545-1556. https://doi.org/10.1021/acsenergylett.8b00553.
122. Guo, Z., Yang, F., Li, X., et al. (2024). Electrocatalytic CO_2 reduction to C_2H_4: From lab to fab. Journal of Energy Chemistry **90**:540-564. https://doi.org/10.1016/j.jechem.2023.11.019.
123. Woldu, A.R., Huang, Z., Zhao, P., et al. (2022). Electrochemical CO_2 reduction (CO_2RR) to multi-carbon products over copper-based catalysts. Coordination Chemistry Reviews **454**:214340. https://doi.org/10.1016/j.ccr.2021.214340.
124. Chen, P.-C., Chen, C., Yang, Y., et al. (2023). Chemical and structural evolution of AgCu catalysts in electrochemical CO_2 reduction. Journal of the American Chemical Society **145**(18):10116-10125. https://doi.org/10.1021/jacs.3c00467.
125. Mustapha, U., Nnadiekwe, C.C., Alhaboudal, M.A., et al. (2023). The role of morphology on the electrochemical CO_2 reduction performance of transition metal-based catalysts. Journal of Energy Chemistry **85**:198-219. https://doi.org/10.1016/j.jechem.2023.06.010.
126. Wu, Q., Du, R., Wang, P., et al. (2023). Nanograin-boundary-abundant Cu_2O-Cu nanocubes with High C_{2+} selectivity and good stability during electrochemical CO_2 reduction at a current density of 500 mA/cm^2. ACS Nano **17**(13):12884-12894. https://doi.org/10.1021/acsnano.3c04951.
127. Yusuf, B.A., Yaseen, W., Meng, S., et al. (2023). Insights into the dynamic evolution of catalytic active centers of the electrocatalytic carbon dioxide reduction reaction. Coordination Chemistry Reviews **492**:215273. https://doi.org/10.1016/j.ccr.2023.215273.
128. Han, C., Kundi, V., Ma, Z., et al. (2023). Differentiating the impacts of Cu_2O initial low- and high-index facets on their reconstruction and catalytic performance in electrochemical CO_2 reduction reaction. Advanced Functional Materials **33**(12):2210938. https://doi.org/10.1002/adfm.202210938.
129. Lai, W., Qiao, Y., Wang, Y., and Huang, H. (2023). Stability issues in electrochemical CO_2 reduction: Recent advances in fundamental understanding and design strategies. Advanced Materials **35**(51):2306288. https://doi.org/10.1002/adma.202306288.
130. Qu, J., Cao, X., Gao, L., et al. (2023). Electrochemical carbon dioxide reduction to ethylene: From mechanistic understanding to catalyst surface engineering. Nano-Micro Letters **15**(1):178. https://doi.org/10.1007/s40820-023-01146-x.
131. Liu, F., Wang, J., Ren, X., et al. (2024). In-situ reconstructed In doped SnO_2 amorphous–crystalline heterostructure for highly efficient CO_2 electroreduction with a dynamic structure-function relationship. Applied Catalysis B: Environment and Energy **352**:124004. https://doi.org/10.1016/j.apcatb.2024.124004.
132. Luo, X., Tan, X., Ji, P., et al. (2023). Surface reconstruction-derived heterostructures for electrochemical water splitting. EnergyChem **5**(2):100091. https://doi.org/10.1016/j.enchem.2022.100091.
133. Zhang, Y., Liu, H., Zhao, S., et al. (2023). Insights into the dynamic evolution of defects in electrocatalysts. Advanced Materials **35**(9):2209680. https://doi.org/10.1002/adma.202209680.
134. Yuan, L.-J., Sui, X.-L., Liu, C., et al. (2023). Electrocatalysis mechanism and structure–activity relationship of atomically dispersed metal-nitrogen-carbon catalysts for electrocatalytic reactions. Small Methods **7**(3):2201524. https://doi.org/10.1002/smtd.202201524.
135. Zhao, S., Yang, Y., and Tang, Z. (2022). Insight into structural evolution, active sites, and stability of heterogeneous electrocatalysts. Angewandte Chemie International Edition **61**(11):e202110186. https://doi.org/10.1002/anie.202110186.
136. Yang, Z.-W., Chen, J.-M., Qiu, L.-Q., et al. (2022). Molecular engineering of metal complexes for

electrocatalytic carbon dioxide reduction: From adjustment of intrinsic activity to molecular immobilization. Angewandte Chemie International Edition **61**(44):e202205301. https://doi.org/10.1002/anie.202205301.

137. Yu, M., Sui, P.-F., Fu, X.-Z., et al. (2023). Specific metal nanostructures toward electrochemical CO_2 reduction: Recent Advances and perspectives. Advanced Energy Materials **13**(2):2203191. https://doi.org/10.1002/aenm.202203191.
138. Li, M., Wang, H., Luo, W., et al. (2020). Heterogeneous single-atom catalysts for electrochemical CO_2 reduction reaction. Advanced Materials **32**(34):2001848. https://doi.org/10.1002/adma.202001848.
139. Zhang, Q., and Guan, J. (2020). Single-atom catalysts for electrocatalytic applications. Advanced Functional Materials **30**(31):2000768. https://doi.org/10.1002/adfm.202000768.
140. Guo, Z., Zhu, H., Yang, G., et al. (2023). Synergistic engineering of heteronuclear Ni-Ag dual-atom catalysts for high-efficiency CO_2 electroreduction with nearly 100% CO selectivity. Chemical Engineering Journal **476**:146556. https://doi.org/10.1016/j.cej.2023.146556.
141. Zhang, J., Cai, W., Hu, F.X., et al. (2021). Recent advances in single atom catalysts for the electrochemical carbon dioxide reduction reaction. Chemical Science **12**(20):6800-6819. https://doi.org/10.1039/D1SC01375K.
142. Wang, H., Tong, Y., and Chen, P. (2023). Microenvironment regulation strategies of single-atom catalysts for advanced electrocatalytic CO_2 reduction to CO. Nano Energy **118**:108967. https://doi.org/10.1016/j.nanoen.2023.108967.
143. Lin, S.-C., Chang, C.-C., Chiu, S.-Y., et al. (2020). Operando time-resolved X-ray absorption spectroscopy reveals the chemical nature enabling highly selective CO_2 reduction. Nature Communications **11**(1):3525. https://doi.org/10.1038/s41467-020-17231-3.
144. Zhu, Y., Kuo, T.-R., Li, Y.-H., et al. (2021). Emerging dynamic structure of electrocatalysts unveiled by in situ X-ray diffraction/absorption spectroscopy. Energy & Environmental Science **14**(4):1928-1958. https://doi.org/10.1039/D0EE03903A.
145. Cai, Z., Cao, N., Zhang, F., et al. (2023). Hierarchical Ag-Cu interfaces promote C-C coupling in tandem CO_2 electroreduction. Applied Catalysis B: Environmental **325**:122310. https://doi.org/10.1016/j.apcatb.2022.122310.
146. Liang, Y., Zhao, J., Yang, Y., et al. (2023). Stabilizing copper sites in coordination polymers toward efficient electrochemical C-C coupling. Nature Communications **14**(1):474. https://doi.org/10.1038/s41467-023-35993-4.
147. Xia, W., Xie, Y., Jia, S., et al. (2023). Adjacent copper single atoms promote C–C coupling in electrochemical CO_2 reduction for the efficient conversion of ethanol. Journal of the American Chemical Society **145**(31):17253-17264. https://doi.org/10.1021/jacs.3c04612.
148. Chang, C.-J., Lai, Y.-A., Chu, Y.-C., et al. (2023). Lewis acidic support boosts C–C coupling in the pulsed electrochemical CO_2 reaction. Journal of the American Chemical Society **145**(12):6953-6965. https://doi.org/10.1021/jacs.3c00472.
149. Wang, Y., Yang, F., Xu, H., et al. (2024). The role of phase mixing degree in promoting C−C coupling in electrochemical CO_2 reduction reaction on Cu-based catalysts. Angewandte Chemie International Edition **63**(16):e202400952. https://doi.org/10.1002/anie.202400952.
150. Finšgar, M., and Milošev, I. (2010). Inhibition of copper corrosion by 1,2,3-benzotriazole: A review. Corrosion Science **52**(9):2737-2749. https://doi.org/10.1016/j.corsci.2010.05.002.
151. He, Y., Liu, S., Wang, M., et al. (2023). Advanced in situ characterization techniques for direct observation of gas-involved electrochemical reactions. Energy & Environmental Materials **6**(6):e12552. https://doi.org/10.1002/eem2.12552.
152. Chen, M., Liu, D., Qiao, L., et al. (2023). In-situ/operando Raman techniques for in-depth understanding on electrocatalysis. Chemical Engineering Journal **461**:141939. https://doi.org/10.1016/j.cej.2023.141939.

153. Li, H., Wei, P., Gao, D., and Wang, G. (2022). In situ Raman spectroscopy studies for electrochemical CO_2 reduction over Cu catalysts. Current Opinion in Green and Sustainable Chemistry **34**:100589. https://doi.org/10.1016/j.cogsc.2022.100589.

154. Yang, Y., Feijóo, J., Briega-Martos, V., et al. (2023). Operando methods: A new era of electrochemistry. Current Opinion in Electrochemistry **42**:101403. https://doi.org/10.1016/j.coelec.2023.101403.

155. Yang, Y., Shao, Y.-T., Abruña, H.D., et al. (2023). Operando electrochemical liquid-cell 4D-STEM studies of dynamic evolution of Cu nanocatalysts for CO_2 reduction. Microscopy and Microanalysis **29**(Supplement_1):1300-1301. https://doi.org/10.1093/micmic/ozad067.665.

156. Gong, Y., and He, T. (2023). Gaining deep understanding of electrochemical CO_2RR with in situ/operando techniques. Small Methods **7**(11):2300702. https://doi.org/10.1002/smtd.202300702.

157. Lee, S.H., Lin, J.C., Farmand, M., et al. (2021). Oxidation state and surface reconstruction of Cu under CO_2 reduction conditions from in situ X-ray characterization. Journal of the American Chemical Society **143**(2):588-592. https://doi.org/10.1021/jacs.0c10017.

158. Liu, Q., Jiang, Q., Li, L., and Yang, W. (2024). Spontaneous reconstruction of copper active sites during the alkaline CORR: Degradation and recovery of the performance. Journal of the American Chemical Society **146**(6):4242-4251. https://doi.org/10.1021/jacs.3c14129.

159. Zhao, Y., Tan, X., Yang, W., et al. (2020). Surface reconstruction of ultrathin palladium nanosheets during electrocatalytic CO_2 reduction. Angewandte Chemie International Edition **59**(48):21493-21498. https://doi.org/10.1002/anie.202009616.

160. Popović, S., Smiljanić, M., Jovanovič, P., et al. (2020). Stability and degradation mechanisms of copper-based catalysts for electrochemical CO_2 reduction. Angewandte Chemie International Edition **59**(35):14736-14746. https://doi.org/10.1002/anie.202000617.

161. Jovanovič, P., Hodnik, N., Ruiz-Zepeda, F., et al. (2017). Electrochemical dissolution of iridium and iridium oxide particles in acidic media: Transmission electron microscopy, electrochemical flow cell coupled to inductively coupled plasma mass spectrometry, and X-ray absorption spectroscopy study. Journal of the American Chemical Society **139**(36):12837-12846. https://doi.org/10.1021/jacs.7b08071.

162. Spöri, C., Kwan, J.T.H., Bonakdarpour, A., et al. (2017). The stability challenges of oxygen evolving catalysts: Towards a common fundamental understanding and mitigation of catalyst degradation. Angewandte Chemie International Edition **56**(22):5994-6021. https://doi.org/10.1002/anie.201608601.

163. Meier, J.C., Galeano, C., Katsounaros, I., et al. (2012). Degradation mechanisms of Pt/C fuel cell catalysts under simulated start–stop conditions. ACS Catalysis **2**(5):832-843. https://doi.org/10.1021/cs300024h.

164. Rossi, K., and Buonsanti, R. (2022). Shaping copper nanocatalysts to steer selectivity in the electrochemical CO_2 reduction reaction. Accounts of Chemical Research **55**(5):629-637. https://doi.org/10.1021/acs.accounts.1c00673.

165. Wu, Z.-Z., Yang, P.-P., and Gao, M.-R. (2024). Dynamic evolution of copper-based catalysts during CO_2 electroreduction. Nano Materials Science. https://doi.org/10.1016/j.nanoms.2024.01.007.

166. Speck, F.D., and Cherevko, S. (2020). Electrochemical copper dissolution: A benchmark for stable CO_2 reduction on copper electrocatalysts. Electrochemistry Communications **115**:106739. https://doi.org/10.1016/j.elecom.2020.106739.

167. Li, F.-M., Huang, L., Zaman, S., et al. (2022). Corrosion chemistry of electrocatalysts. Advanced Materials **34**(52):2200840. https://doi.org/10.1002/adma.202200840.

168. Wang, F., Lu, Z., Guo, H., et al. (2024). Copper-based catalysts for CO_2 electroreduction to $C_2/_{2+}$ products: Advance and perspective. Coordination Chemistry Reviews **515**:215962. https://doi.org/10.1016/j.ccr.2024.215962.

169. Ma, W., Xie, S., Liu, T., et al. (2020). Electrocatalytic reduction of CO_2 to ethylene and ethanol through

hydrogen-assisted C–C coupling over fluorine-modified copper. Nature Catalysis **3**(6):478-487. https://doi.org/10.1038/s41929-020-0450-0.

170. Li, H., Liu, T., Wei, P., et al. (2021). High-rate CO_2 electroreduction to C_{2+} products over a copper-copper iodide catalyst. Angewandte Chemie International Edition **60**(26):14329-14333. https://doi.org/10.1002/anie.202102657.
171. Gao, D., Sinev, I., Scholten, F., et al. (2019). Selective CO_2 electroreduction to ethylene and multicarbon alcohols via electrolyte-driven nanostructuring. Angewandte Chemie International Edition **58**(47):17047-17053. https://doi.org/10.1002/anie.201910155.
172. Li, M., Ma, Y., Chen, J., et al. (2021). Residual chlorine induced cationic active species on a porous copper electrocatalyst for highly stable electrochemical CO_2 reduction to C_{2+}. Angewandte Chemie International Edition **60**(20):11487-11493. https://doi.org/10.1002/anie.202102606.
173. Wang, J., Yang, H., Liu, Q., et al. (2021). Fastening Br– ions at copper–molecule interface enables highly efficient electroreduction of CO_2 to ethanol. ACS Energy Letters **6**(2):437-444. https://doi.org/10.1021/acsenergylett.0c02364.
174. Cai, R., Sun, M., Ren, J., et al. (2021). Unexpected high selectivity for acetate formation from CO_2 reduction with copper based 2D hybrid catalysts at ultralow potentials. Chemical Science **12**(46):15382-15388. https://doi.org/10.1039/D1SC05441D.
175. Holtz, M.E., Yu, Y., Gunceler, D., et al. (2014). Nanoscale imaging of lithium ion distribution during in situ operation of battery electrode and electrolyte. Nano Letters **14**(3):1453-1459. https://doi.org/10.1021/nl404577c.
176. Holtz, M.E., Yu, Y., Gao, J., et al. (2013). In situ electron energy-loss spectroscopy in liquids. Microscopy and Microanalysis **19**(4):1027-1035. https://doi.org/10.1017/S1431927613001505
177. Klein, K., de Jonge, N., and Anderson, I. (2011). Energy-loss characteristics for EFTEM imaging with a liquid flow cell. Microscopy and Microanalysis **17**(S2):780-781. https://doi.org/10.1017/S1431927611004776.
178. Jungjohann, K.L., Evans, J.E., Aguiar, J.A., et al. (2012). Atomic-scale imaging and spectroscopy for in situ liquid scanning transmission electron microscopy. Microscopy and Microanalysis **18**(3):621-627. https://doi.org/10.1017/S1431927612000104.
179. Jia, G., Wang, Y., Sun, M., et al. (2023). Size effects of highly dispersed bismuth nanoparticles on electrocatalytic reduction of carbon dioxide to formic acid. Journal of the American Chemical Society **145**(25):14133-14142. https://doi.org/10.1021/jacs.3c04727.
180. Liu, X., Zheng, H., Sun, Q., et al. (2024). Mastering the lattice strain in bismuth-based electrocatalysts for efficient CO_2-to-formate conversion. Advanced Functional Materials **n/a**(n/a):2400928. https://doi.org/10.1002/adfm.202400928.
181. Shen, H., Wang, T., Jiang, H., et al. (2023). Theoretical calculation guided design of single atom-alloyed bismuth catalysts for ampere-level CO_2 electrolysis to formate. Applied Catalysis B: Environmental **339**:123140. https://doi.org/10.1016/j.apcatb.2023.123140.
182. Jiang, Z., Zhang, M., Chen, X., et al. (2023). A bismuth-based zeolitic organic framework with coordination-linked metal cages for efficient electrocatalytic CO_2 reduction to HCOOH. Angewandte Chemie International Edition **62**(45):e202311223. https://doi.org/10.1002/anie.202311223.
183. Wang, H., Tang, C., Sun, B., et al. (2022). In-situ structural evolution of Bi_2O_3 nanoparticle catalysts for CO_2 electroreduction. International Journal of Extreme Manufacturing **4**(3):035002. https://doi.org/10.1088/2631-7990/ac7a6e.
184. Lee, J., Liu, H., Chen, Y., and Li, W. (2022). Bismuth nanosheets derived by in situ morphology transformation of bismuth oxides for selective electrochemical CO_2 reduction to formate. ACS Applied Materials & Interfaces **14**(12):14210-14217. https://doi.org/10.1021/acsami.1c25217.
185. Serra-Maia, R., Kumar, P., Meng, A.C., et al. (2021). Nanoscale chemical and structural analysis during in situ scanning/transmission electron microscopy in liquids. ACS Nano **15**(6):10228-10240.

https://doi.org/10.1021/acsnano.1c02340.

186. Impagnatiello, A., Cerqueira, C.F., Coulon, P.-E., et al. (2020). Degradation mechanisms of supported Pt nanocatalysts in proton exchange membrane fuel cells: An operando study through liquid cell transmission electron microscopy. ACS Applied Energy Materials **3**(3):2360-2371. https://doi.org/10.1021/acsaem.9b02000.

187. Vlassak, J.J., and Nix, W.D. (1992). A new bulge test technique for the determination of Young's modulus and Poisson's ratio of thin films. Journal of Materials Research **7**(12):3242-3249. https://doi.org/10.1557/JMR.1992.3242.

188. Yesibolati, M.N., Laganá, S., Kadkhodazadeh, S., et al. (2020). Electron inelastic mean free path in water. Nanoscale **12**(40):20649-20657. https://doi.org/10.1039/D0NR04352D.

189. Egerton, R.F. (2011). TEM Applications of EELS. In Electron Energy-Loss Spectroscopy in the Electron Microscope, R.F. Egerton, ed. (Springer US), pp. 293-397. https://doi.org/10.1007/978-1-4419-9583-4_5.

190. Woehl, T.J., Jungjohann, K.L., Evans, J.E., et al. (2013). Experimental procedures to mitigate electron beam induced artifacts during in situ fluid imaging of nanomaterials. Ultramicroscopy **127**:53-63. https://doi.org/10.1016/j.ultramic.2012.07.018.

191. Schneider, N.M., Norton, M.M., Mendel, B.J., et al. (2014). Electron–water interactions and implications for liquid cell electron microscopy. The Journal of Physical Chemistry C **118**(38):22373-22382. https://doi.org/10.1021/jp507400n.

192. Rehn, S.M., and Jones, M.R. (2018). New strategies for probing energy systems with in situ liquid-phase transmission electron microscopy. ACS Energy Letters **3**(6):1269-1278. https://doi.org/10.1021/acsenergylett.8b00527.

193. Lee, D., Betzler, S.B., and Zheng, H. (2024). Characterization of electron beam effects in liquid phase TEM study of chemical processes. Microscopy and Microanalysis **30**(Supplement_1):ozae044.804. https://doi.org/10.1093/mam/ozae044.804.

194. Beermann, V., Holtz, M.E., Padgett, E., et al. (2019). Real-time imaging of activation and degradation of carbon supported octahedral Pt–Ni alloy fuel cell catalysts at the nanoscale using in situ electrochemical liquid cell STEM. Energy & Environmental Science **12**(8):2476-2485. https://doi.org/10.1039/C9EE01185D.

195. Sutter, E., Jungjohann, K., Bliznakov, S., et al. (2014). In situ liquid-cell electron microscopy of silver–palladium galvanic replacement reactions on silver nanoparticles. Nature Communications **5**(1):4946. https://doi.org/10.1038/ncomms5946.

196. Korpanty, J., Parent, L.R., and Gianneschi, N.C. (2021). Enhancing and mitigating radiolytic damage to soft matter in aqueous phase liquid-cell transmission electron microscopy in the presence of gold nanoparticle sensitizers or isopropanol scavengers. Nano Letters **21**(2):1141-1149. https://doi.org/10.1021/acs.nanolett.0c04636.

197. Zheng, H., Claridge, S.A., Minor, A.M., et al. (2009). Nanocrystal diffusion in a liquid thin film observed by in situ transmission electron microscopy. Nano Letters **9**(6):2460-2465. https://doi.org/10.1021/nl9012369.

198. Guth, U., Gerlach, F., Decker, M., et al. (2009). Solid-state reference electrodes for potentiometric sensors. Journal of Solid State Electrochemistry **13**(1):27-39. https://doi.org/10.1007/s10008-008-0574-7.

199. Alnoush, W., Black, R., and Higgins, D. (2021). Judicious selection, validation, and use of reference electrodes for in situ and operando electrocatalysis studies. Chem Catalysis **1**(5):997-1013. https://doi.org/10.1016/j.checat.2021.07.001.

200. Casebolt, R., Levine, K., Suntivich, J., and Hanrath, T. (2021). Pulse check: Potential opportunities in pulsed electrochemical CO_2 reduction. Joule **5**(8):1987-2026. https://doi.org/10.1016/j.joule.2021.05.014.

201. Kim, C., Weng, L.-C., and Bell, A.T. (2020). Impact of pulsed electrochemical reduction of CO_2 on the formation of C_{2+} products over Cu. ACS Catalysis **10**(21):12403-12413. https://doi.org/10.1021/acscatal.0c02915.

202. Li, Z., Wang, L., Wang, T., et al. (2023). Steering the dynamics of reaction intermediates and catalyst surface during electrochemical pulsed CO_2 reduction for enhanced C_{2+} selectivity. Journal of the American Chemical Society **145**(37):20655-20664. https://doi.org/10.1021/jacs.3c08005.

203. Leung, K.Y., and McCrory, C.C.L. (2019). Effect and prevention of trace Ag^+ contamination from Ag/AgCl reference electrodes on CO_2 reduction product distributions at polycrystalline copper electrodes. ACS Applied Energy Materials **2**(11):8283-8293. https://doi.org/10.1021/acsaem.9b01759.

204. Niu, Z.-Z., Chi, L.-P., Liu, R., et al. (2021). Rigorous assessment of CO_2 electroreduction products in a flow cell. Energy & Environmental Science **14**(8):4169-4176. https://doi.org/10.1039/D1EE01664D.

205. Zhao, S., Qin, Y., Wang, X., et al. (2023). Anion exchange facilitates the in situ construction of Bi/Bi–O interfaces for enhanced electrochemical CO_2-to-formate conversion over a wide potential window. Small **19**(43):2302878. https://doi.org/10.1002/smll.202302878.

206. Heenan, A.R., Hamonnet, J., and Marshall, A.T. (2022). Why careful iR compensation and reporting of electrode potentials are critical for the CO_2 reduction reaction. ACS Energy Letters **7**(7):2357-2361. https://doi.org/10.1021/acsenergylett.2c00800.

207. Simon, G.H., Kley, C.S., and Roldan Cuenya, B. (2021). Potential-dependent morphology of copper catalysts during CO_2 electroreduction revealed by in situ atomic force microscopy. Angewandte Chemie International Edition **60**(5):2561-2568. https://doi.org/10.1002/anie.202010449.

208. Banerjee, S., Gerke, C.S., and Thoi, V.S. (2022). Guiding CO_2RR selectivity by compositional tuning in the electrochemical double layer. Accounts of Chemical Research **55**(4):504-515. https://doi.org/10.1021/acs.accounts.1c00680.

209. Mefford, J.T., Akbashev, A.R., Kang, M., et al. (2021). Correlative operando microscopy of oxygen evolution electrocatalysts. Nature **593**(7857):67-73. https://doi.org/10.1038/s41586-021-03454-x.

210. Beker, A.F., Sun, H., Lemang, M., et al. (2020). In situ electrochemistry inside a TEM with controlled mass transport. Nanoscale **12**(43):22192-22201. https://doi.org/10.1039/D0NR04961A.

211. Wu, H., Su, H., Joosten, R.R.M., et al. (2021). Mapping and controlling liquid layer thickness in liquid-phase (scanning) transmission electron microscopy. Small Methods **5**(6):2001287. https://doi.org/10.1002/smtd.202001287.

212. Merkens, S., De Salvo, G., Kruse, J., et al. (2023). Quantification of reagent mixing in liquid flow cells for liquid phase-TEM. Ultramicroscopy **245**:113654. https://doi.org/10.1016/j.ultramic.2022.113654.

213. Lott, T.S., Petruk, A.A., Shaw, N.A., et al. (2023). Robust fully controlled nanometer liquid layers for high resolution liquid-cell electron microscopy. Lab on a Chip **23**(14):3217-3225. https://doi.org/10.1039/D3LC00190C.

214. Koo, K., Li, Z., Liu, Y., et al. (2024). Ultrathin silicon nitride microchip for in situ/operando microscopy with high spatial resolution and spectral visibility. Science Advances **10**(3):eadj6417. https://doi.org/10.1126/sciadv.adj6417.

215. Koo, K., Park, J., Ji, S., et al. (2021). Liquid-flowing graphene chip-based high-resolution electron microscopy. Advanced Materials **33**(2):2005468. https://doi.org/10.1002/adma.202005468.

216. Jensen, E., Burrows, A., and Mølhave, K. (2014). Monolithic chip system with a microfluidic channel for in situ electron microscopy of liquids. Microscopy and Microanalysis **20**(2):445-451. https://doi.org/10.1017/S1431927614000300.

217. Gong, Q., Ding, P., Xu, M., et al. (2019). Structural defects on converted bismuth oxide nanotubes enable highly active electrocatalysis of carbon dioxide reduction. Nature Communications **10**(1):2807. https://doi.org/10.1038/s41467-019-10819-4.

218. Philipp, H.T., Tate, M.W., Shanks, K.S., et al. (2022). Very-high dynamic range, 10,000 frames/second

pixel array detector for electron microscopy. Microscopy and Microanalysis **28**(2):425-440. https://doi.org/10.1017/S1431927622000174.

219. Padgett, E., Holtz, M.E., Cueva, P., et al. (2020). The exit-wave power-cepstrum transform for scanning nanobeam electron diffraction: Robust strain mapping at subnanometer resolution and subpicometer precision. Ultramicroscopy **214**:112994. https://doi.org/10.1016/j.ultramic.2020.112994.
220. Yang, Y., Shao, Y.-T., Lu, X., et al. (2022). Elucidating cathodic corrosion mechanisms with operando electrochemical transmission electron microscopy. Journal of the American Chemical Society **144**(34):15698-15708. https://doi.org/10.1021/jacs.2c05989.
221. Cheng, Z., Wang, C., Wu, X., and Chu, J. (2022). Review in situ transmission electron microscope with machine learning. Journal of Semiconductors **43**(8):081001. https://doi.org/10.1088/1674-4926/43/8/081001.
222. Botifoll, M., Pinto-Huguet, I., and Arbiol, J. (2022). Machine learning in electron microscopy for advanced nanocharacterization: Current developments, available tools and future outlook. Nanoscale Horizons **7**(12):1427-1477. https://doi.org/10.1039/D2NH00377E.
223. Ziatdinov, M., Dyck, O., Maksov, A., et al. (2017). Deep learning of atomically resolved scanning transmission electron microscopy images: Chemical identification and tracking local transformations. ACS Nano **11**(12):12742-12752. https://doi.org/10.1021/acsnano.7b07504.
224. Ziletti, A., Kumar, D., Scheffler, M., and Ghiringhelli, L.M. (2018). Insightful classification of crystal structures using deep learning. Nature Communications **9**(1):2775. https://doi.org/10.1038/s41467-018-05169-6.
225. Förster, G.D., Castan, A., Loiseau, A., et al. (2020). A deep learning approach for determining the chiral indices of carbon nanotubes from high-resolution transmission electron microscopy images. Carbon **169**:465-474. https://doi.org/10.1016/j.carbon.2020.06.086.
226. Gumbiowski, N., Loza, K., Heggen, M., and Epple, M. (2023). Automated analysis of transmission electron micrographs of metallic nanoparticles by machine learning. Nanoscale Advances **5**(8):2318-2326. https://doi.org/10.1039/D2NA00781A.
227. Roccapriore, K.M., Ziatdinov, M., Cho, S.H., et al. (2021). Predictability of localized plasmonic responses in nanoparticle assemblies. Small **17**(21):2100181. https://doi.org/10.1002/smll.202100181.
228. Zheng, S., Wang, C., Yuan, X., and Xin, H.L. (2021). Super-compression of large electron microscopy time series by deep compressive sensing learning. Patterns **2**(7):100292. https://doi.org/10.1016/j.patter.2021.100292.

Acknowledgments

This work is financially supported by Ningbo Science and Technology Bureau (2021S097), the Department of Science and Technology of Zhejiang Province (LGF22B060009), and the Deutsche Forschungsgemeinschaft (German Research Foundation, 511462370). P.Y. Tang extends gratitude to the Hundred Talents Program of Chinese Academy of Sciences (E2XBRD1001), and Z.Y. Guo acknowledges the University of Nottingham Ningbo China for providing a full PhD scholarship.

Declaration of interests

The authors declare no competing interests.

Author contributions

All authors have given permission for the final version of this manuscript. Conceptualization: P.F. Cao and M.X. Xu; Writing – original draft: Z.Y. Guo, P. Paciok and R. Zandonella; Writing – review & editing: M.X. Xu, P.F. Cao, P.Y. Tang, Z.Y. Guo, Z.Y. Xi, H.W. Zhu, J. Mayer, J. Arbiol, and T. Wu; Supervision: M.X. Xu, P.F. Cao, and P.Y. Tang.

List of figure titles and legends

Figure 1. A concise timeline of *in situ* LC-TEM development on heterogeneous catalysis.[32,43,47,53-56,62,68]

Figure 2. Schematic illustration of *in situ* LC-TEM imaging techniques, including (a) Low-vapor-pressure liquid cell (Reproduced with permission from [79]. Copyright 2017 Elsevier.), (b) TEM with differential pumping (Reproduced with permission from [86]. Copyright 2014 Elsevier.), (c) Microchip liquid cell (Reproduced with permission from [94]. Copyright 2019 Wiley-VCH.), and (d) Graphene liquid cell. (Reproduced with permission from [56]. Copyright 2012, American Association for the Advancement of Science.)

Figure 3. (a-d) *In situ* STEM images of the working electrode of cubic Cu_2O at various times during the experiment: (a) t = 1 s, (b) t = 61 s, (c) t = 246 s, and (d) t = 750 s. The potential was applied at −0.7 V vs. Pt pseudo-reference. The scale bar represents 1 µm. Overview of an electrochemical cell setup: (e) a cross-section of the LC-TEM at the top, (f) a bottom view of the electrodes on the electrochemistry chip at the bottom, and (g) an SEM image of the working electrode in the liquid cell. The dashed box indicates the size of the top window. (Reproduced with permission from [32]. Copyright 2020, The Authors Springer Nature). *In situ* LC-TEM images showing the morphological evolution of Cu_2O cubes of different sizes: (h-k) 390 nm, (l-o) 170 nm, and (p-s) 80 nm, after applying a potential of −0.9 V vs. RHE over 45 min of CO_2RR by LC-TEM. (t) Partial current densities for H_2, CO, CH_4, and C_2H_4, obtained from time-resolved gas chromatography data over 12 h. (Reproduced with permission from [31]. Copyright 2021, The Authors Springer Nature.)

Figure 4. *In situ* TEM images of CuO nanosheet (NS) catalyst morphology during OCP at (a) 2 s, (b) 50 s and (c) 110 s. (d) Current/potential (vs. RHE and vs. Pt) profiles over time during first linear sweep voltammetry (LSV) coupled with chronoamperometry (CA) measurements with marked time points, t_1-t_4 (vertical lines). (e-h) Corresponding to *in situ* TEM images in (d). *In situ* TEM snapshot sequence during (i-j) the second LSV coupled with CA at −1.23 V vs. RHE, and (k-l) during the third LSV coupled with CA at −1.73 V vs. RHE. (Reproduced with permission from [29]. Copyright 2021, The Authors Springer Nature)

Figure 5. (a1-a5) *In situ* dark-field STEM images of as-prepared Cu SACs at accurately calibrated potentials vs. RHE for various durations ranging from 0 to 160 s. Below are magnified images of the selected area in (a) and line profiles of chosen clusters. (b) Schematic of *in situ* electrochemical LC-TEM and its corresponding electrochemical chip. (Reproduced with permission from [30]. Copyright 2023 The Authors Springer Nature) *Ex situ* electron microscopy of the Cu nanoparticle (NP) ensemble evolution timeline. (c and d) *Ex situ* SEM images after electrode removal at various bias time points (scale bars, 100 nm). (e1) HRTEM (Scale bar: 10 nm) of a single Cu_2O cube at 50 s, alongside (e2) its Fourier transform revealing Cu_2O reflections (Scale bar: 2 nm^{-1}), and (e3) a magnified view of a selected region (Scale bar: 2 nm). (f) *In situ* STEM imaging of the 7-nm Cu NP at −0.6 V vs. the carbon pseudo-reference over a 10 s biasing period. (g) *In situ* STEM imaging of larger Cu NPs (size of 20 nm) during a 60 s biasing period at −0.6 V vs. the carbon pseudo-reference. (Reproduced with permission from [28]. Copyright 2020 National Academy of Sciences.)

Figure 6. (a) Schematic of operando electrochemical LC-STEM. Overview of the life cycle of 7 nm Cu NPs depicted through electrochemical LC-STEM images: (b) initial growth after a single negative-direction LSV scan, ranging from 0.4 to 0 V; (c) further growth under constant applied potential at 0 V; and (d) post-electrolysis formation of Cu_2O cubes (indicated by the arrow) upon exposure to air at the same location. Morphological evolution of 7 nm Cu NPs at 0 V vs. RHE at 0 s (e), 8 s (f), 16 s (g), and 24 s (h). False-color images in the inset of (h) emphasize newly formed regions (highlighted in green) after 24 s of growth. Further aggregation of 7 nm Cu NPs at −0.8 V for 0 s (i), 8 s (j), 16 s (k), and 32 s (l), highlighting significant changes within dashed boxes. (m) False-color dark-field 4D-STEM maps exhibit Cu nanograins with diffraction spots, while specific regions demonstrate (n) loosely connected Cu nanograins and (o) overlapping nanograin boundaries. (p) Representative diffraction patterns of single-crystal-like Cu nanograins. (q) False-color dark-field 4D-STEM images revealing highly crystalline Cu nanograins with diffraction spots similar to those marked as 1, 2, and 3 in (p). (Reproduced with permission from [34]. Copyright 2023 Springer Nature.)

Figure 7. (a) Schematics of the polymer liquid cell (PLC) structure and its assembly. (b) *In situ* TEM image sequences between 0.2 s and 3.2 s at an applied potential of −1.1 V vs. RHE showing the emergence and fluctuation of amorphous interphase. (c) Schematic diagram of the amorphous components affecting the reconstruction of the crystalline Cu surface through dynamic flow and interconversion behavior. (d) *In situ* high-resolution TEM (HRTEM) images of amorphous interphase showing liquid flow from left to right along the crystalline Cu edge from T_0 to T_0 + 3.0 s. Scale bar: 5 nm. (e) *In situ* HRTEM images of the interconversion between crystalline copper and amorphous interphase. Scale bar: 5 nm. (Reproduced with permission from [68]. Copyright 2024 The Authors Springer Nature.)

Figure 8. (a) *In situ* LC-TEM images taken at various times during the experiment, the red and blue frames are magnified in (b) and (c), respectively. (b) Magnified images illustrating the secondary particle growth process (red). (c) Magnified images showing the shrinking process of the primary particles (blue). (d) Electrochemical data recorded *in situ* during the experiment. (e) Evolution of the area-weighted particle size distribution. Arrow I indicates the decline in the population of primary particles, while Arrow II denotes the gradual increase in the population of secondary particles. (f) The mean circular equivalent diameter (black line) ± its standard error (grey), alongside the standard deviation (red) derived from the fitted lognormal distribution, the biasing during CO_2 electrolysis is −0.25 V vs. RHE. (g) Diffractograms at chosen potentials, depicted as rotational averages of the corresponding SAED patterns in panels (h) and (i). (j) Time-resolved diffractograms synchronized with the electrochemical experiment, where selected potentials are represented as horizontal cross-sections from the dataset. (k) Fractions of Cu and Cu_2O components. (l) LSV curve recorded during the experiment. (Reproduced with permission from [36]. Copyright 2020 John Wiley and Sons.)

Figure 9. *In situ* electrochemical Liquid cell high-angle annular dark-field (LC-HADDF) STEM images of copper arrays observed (a) in Milli-Q pure water, (b) in 0.01 M KI after anodization, and (c) in iodine-free CO_2-saturated 0.1 M $KHCO_3$ after 30 minutes under CO_2RR conditions at −1.0 V vs. RHE. (d–g) CuI transforms into Cu filaments under CO_2RR conditions (−1.0 V vs. RHE, iodide-free CO_2-saturated 0.1 M $KHCO_3$). (h–k) Following 30 minutes of CO_2RR, the potential was withdrawn, leading to the re-precipitation of triangular CuI structures at OCP. (Reproduced with permission from [35]. Copyright 2022 Royal Society of Chemistry.)

Figure 10. (a) *In situ* LC-TEM images collected while the samples were in contact with a 0.1 M $KHCO_3$ solution. *In situ* LC-TEM images of the (i) initial and (ii) post-reaction electrocatalysts at constant applied potentials of (b) −0.3 V, (d) −0.4 V, and (f) −0.5 V vs. RHE in CO_2-saturated 1 M $KHCO_3$ solution. (c, e, g) The corresponding current-time (i-t) curves for (b), (d) and (f). The current jumps occurring every 15-20 minutes are a result of pausing the chronoamperometry (CA) test to change the syringe containing the electrolyte, ensuring continuous electrolyte flow. (Reproduced with permission from [38]. Copyright 2024 The Authors American Chemical Society.)

Figure 1

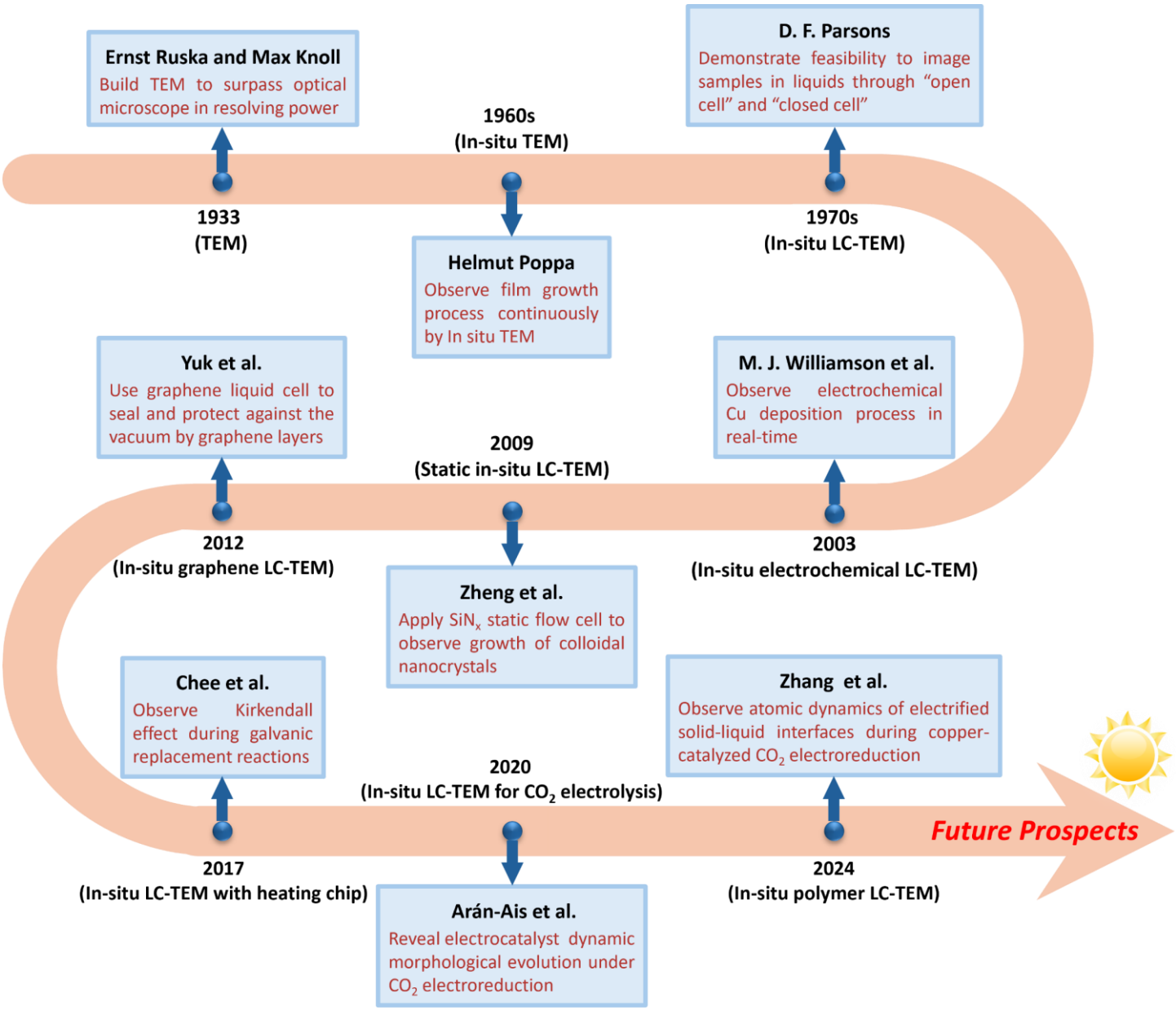
Ernst Ruska and Max Knoll
Build TEM to surpass optical microscope in resolving power
1933
(TEM)
1960s
(In-situ TEM)
Helmut Poppa
Observe film growth process continuously by In situ TEM
D. F. Parsons
Demonstrate feasibility to image samples in liquids through "open cell" and "closed cell"
1970s
(In-situ LC-TEM)
Yuk et al.
Use graphene liquid cell to seal and protect against the vacuum by graphene layers
2012
(In-situ graphene LC-TEM)
2009
(Static in-situ LC-TEM)
Zheng et al.
Apply SiN_x static flow cell to observe growth of colloidal nanocrystals
M. J. Williamson et al.
Observe electrochemical Cu deposition process in real-time
2003
(In-situ electrochemical LC-TEM)
Chee et al.
Observe Kirkendall effect during galvanic replacement reactions
2017
(In-situ LC-TEM with heating chip)
2020
(In-situ LC-TEM for CO_2 electrolysis)
Arán-Ais et al.
Reveal electrocatalyst dynamic morphological evolution under CO_2 electroreduction
Zhang et al.
Observe atomic dynamics of electrified solid-liquid interfaces during copper-catalyzed CO_2 electroreduction
2024
(In-situ polymer LC-TEM)
Future Prospects

Figure 2

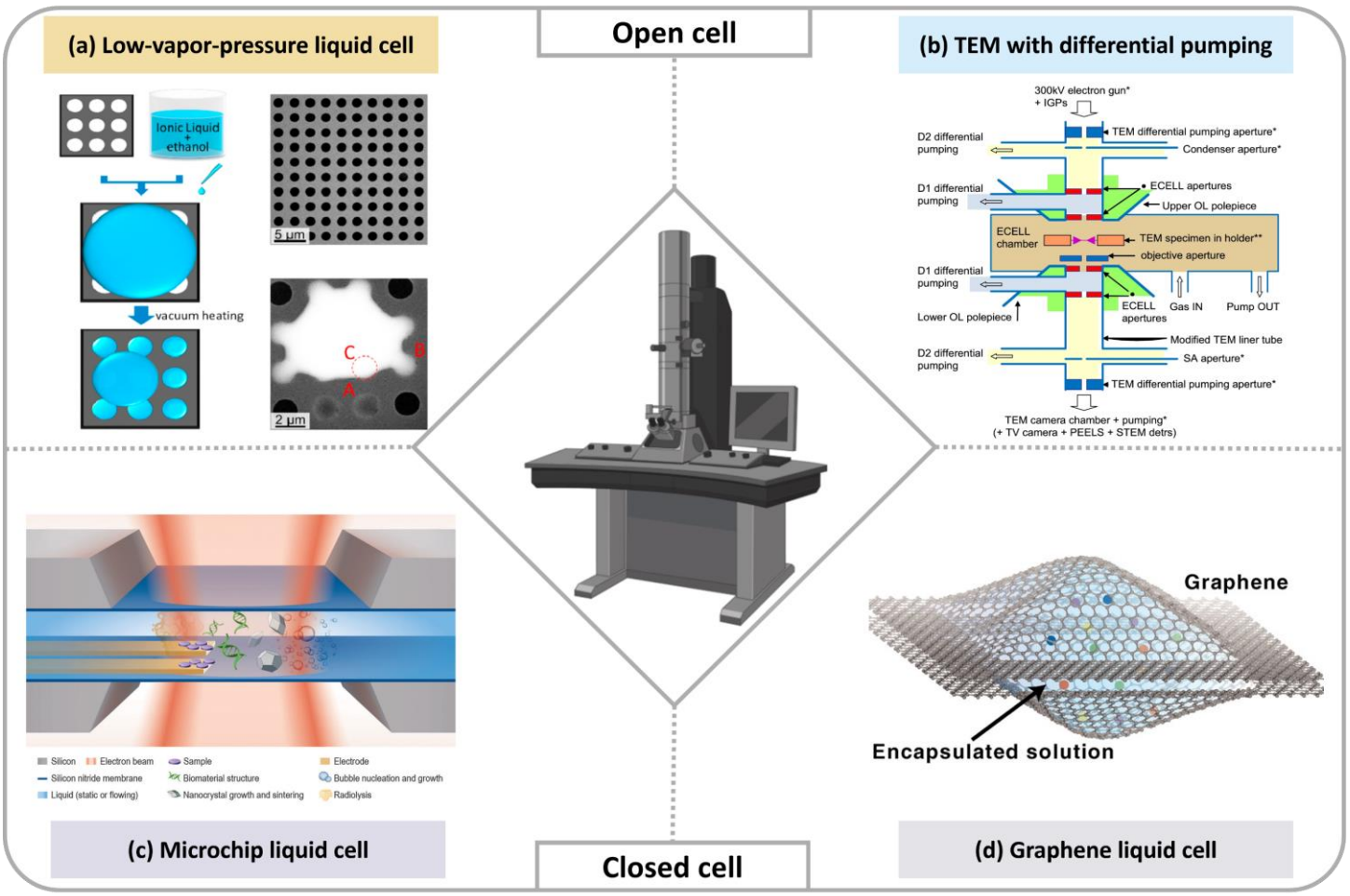
(a) Low-vapor-pressure liquid cell
Ionic Liquid + ethanol
vacuum heating
5 µm
2 µm
C
B
A
Open cell
(b) TEM with differential pumping
300kV electron gun* + IGPs
D2 differential pumping
TEM differential pumping aperture*
Condenser aperture*
D1 differential pumping
ECELL apertures
Upper OL polepiece
ECELL chamber
TEM specimen in holder**
objective aperture
D1 differential pumping
Lower OL polepiece
ECELL apertures
Gas IN
Pump OUT
Modified TEM liner tube
D2 differential pumping
SA aperture*
TEM differential pumping aperture*
TEM camera chamber + pumping*
(+ TV camera + PEELS + STEM detrs)
Silicon
Electron beam
Sample
Electrode
Silicon nitride membrane
Biomaterial structure
Bubble nucleation and growth
Liquid (static or flowing)
Nanocrystal growth and sintering
Radiolysis
(c) Microchip liquid cell
Graphene
Encapsulated solution
(d) Graphene liquid cell
Closed cell

Figure 3

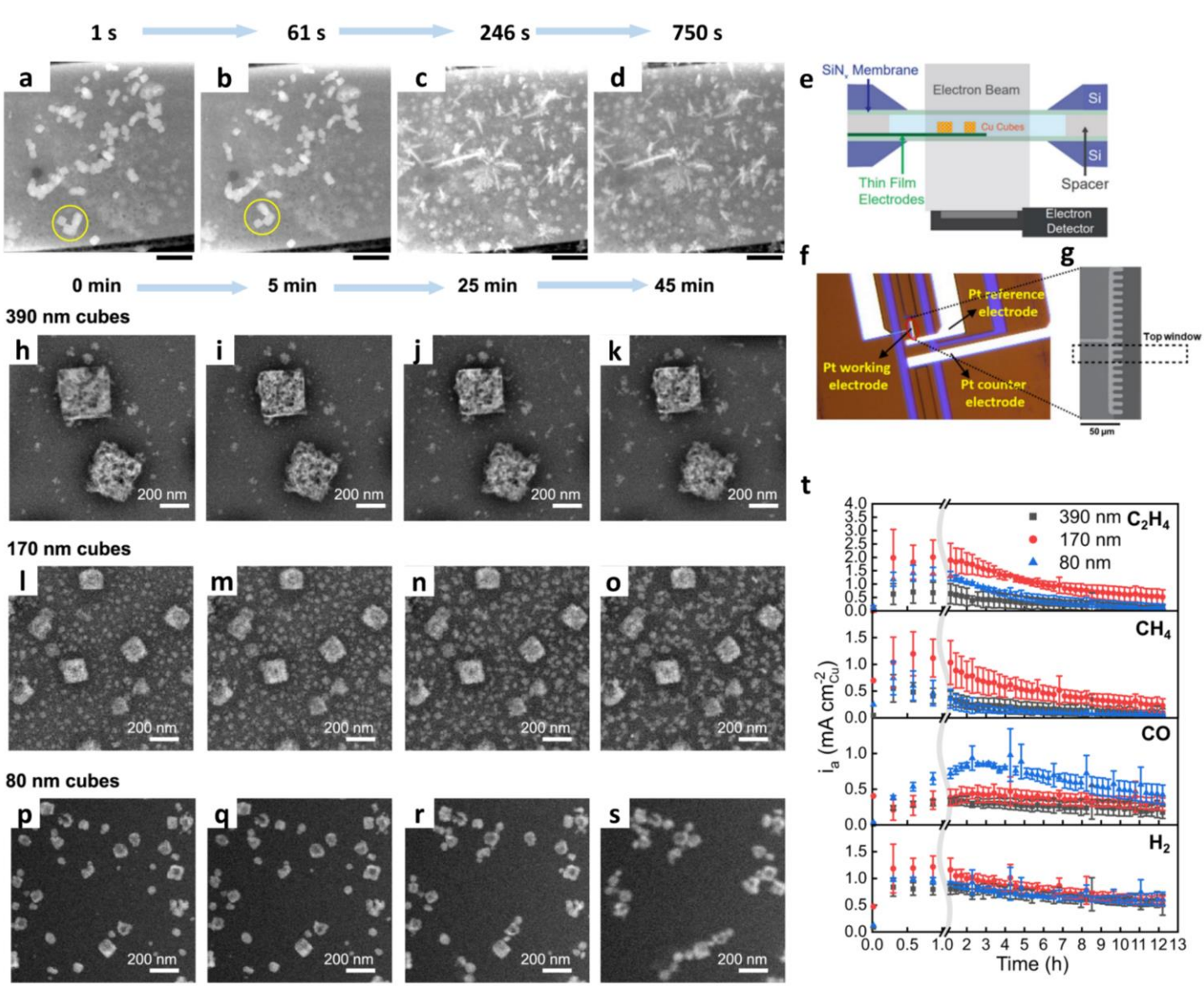
1 s
61 s
246 s
750 s
a
b
c
d
e
SiNx Membrane
Electron Beam
Si
Cu Cubes
Si
Thin Film Electrodes
Spacer
Electron Detector
f
g
Pt reference electrode
Pt working electrode
Pt counter electrode
Top window
50 μm
0 min
5 min
25 min
45 min
390 nm cubes
h
i
j
k
200 nm
170 nm cubes
l
m
n
o
80 nm cubes
p
q
r
s
t
390 nm C2H4
170 nm
80 nm
CH4
CO
H2
ia (mA cm-2Cu)
Time (h)

Figure 4

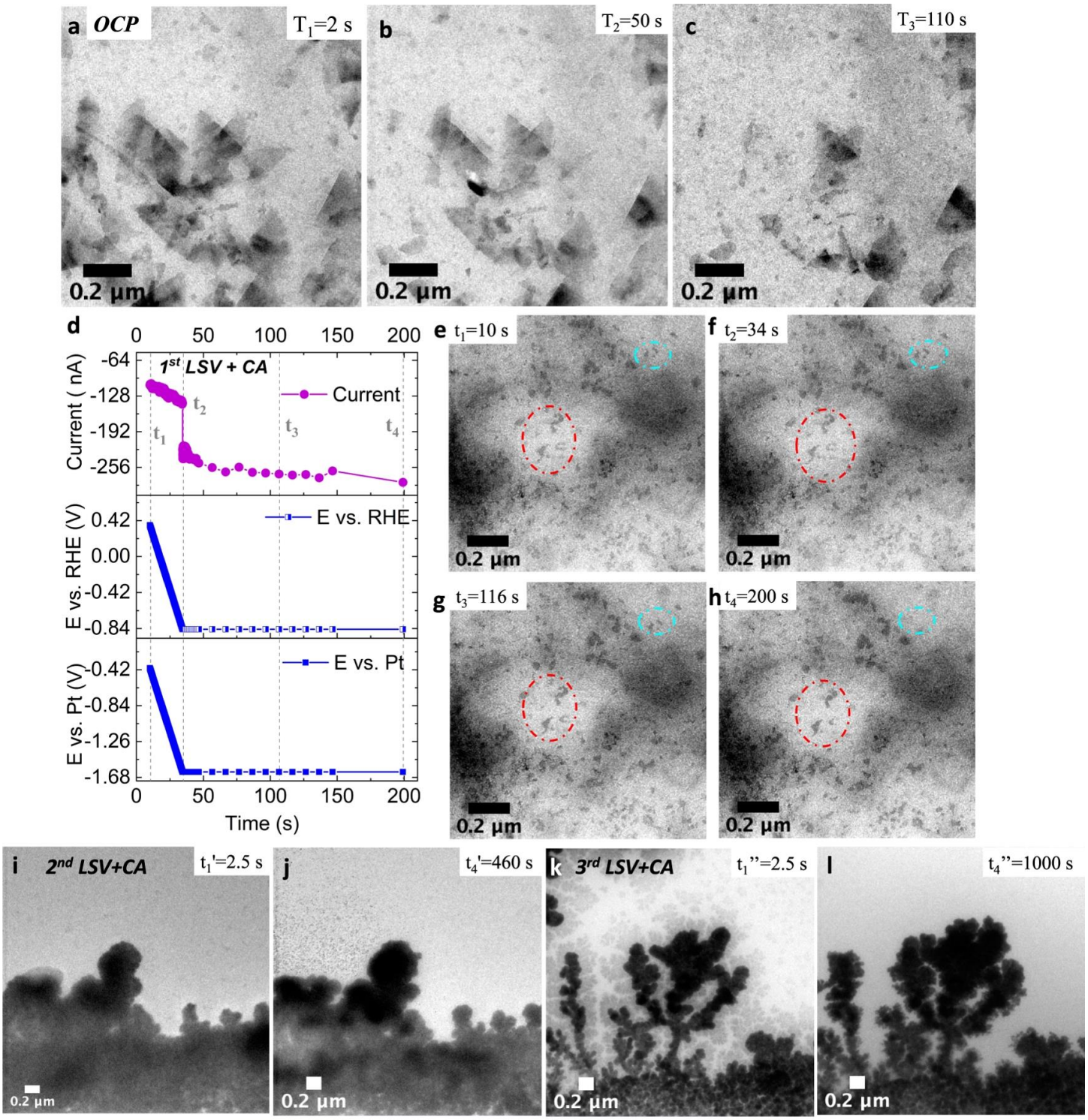
a OCP
T1=2 s
b
T2=50 s
c
T3=110 s
0.2 μm
d
1st LSV + CA
Current (nA)
Current
t1
t2
t3
t4
E vs. RHE (V)
E vs. RHE
E vs. Pt (V)
E vs. Pt
Time (s)
e t1=10 s
f t2=34 s
g t3=116 s
h t4=200 s
i 2nd LSV+CA
t1'=2.5 s
j
t4'=460 s
k 3rd LSV+CA
t1''=2.5 s
l
t4''=1000 s

Figure 5

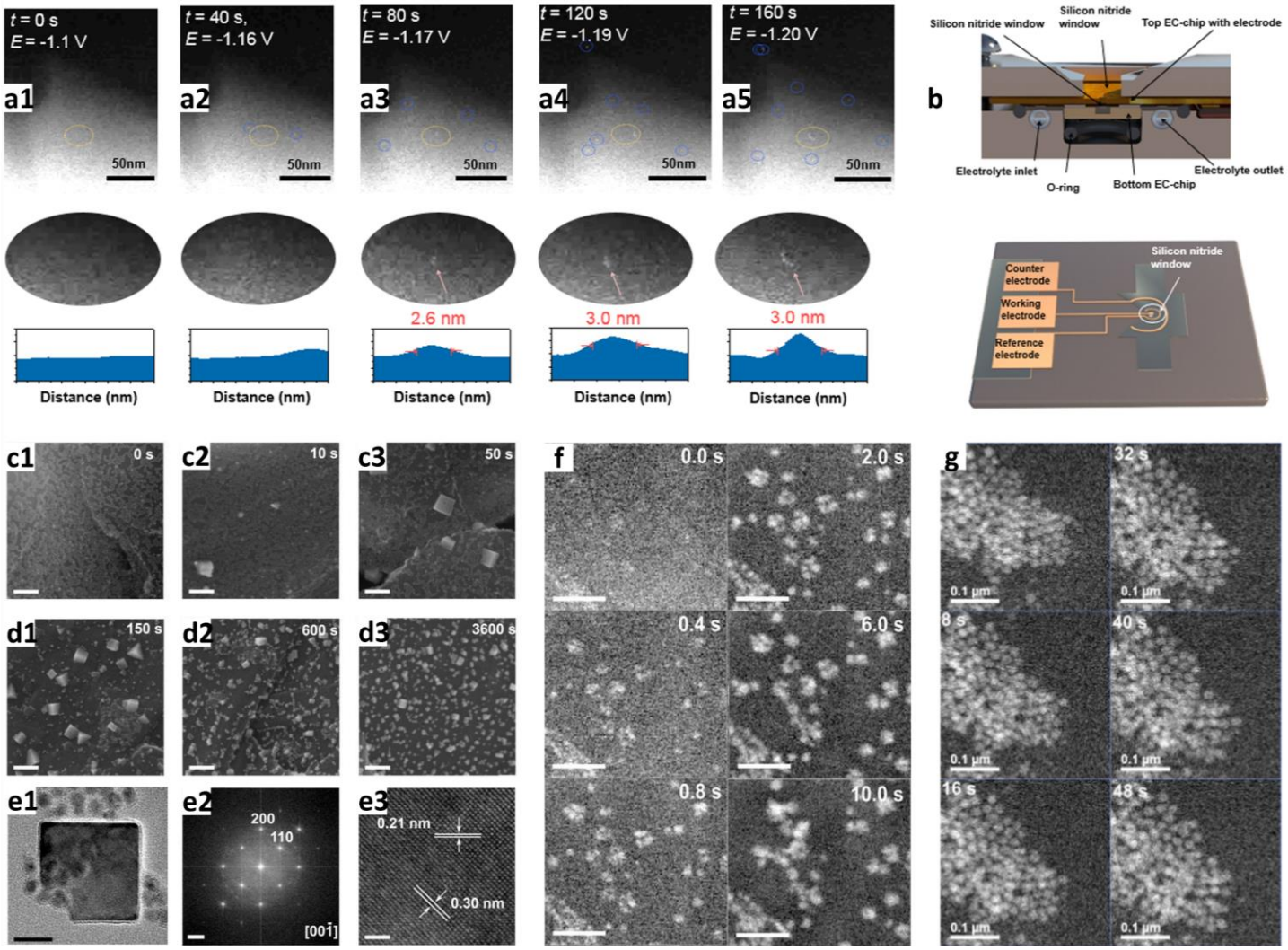
t = 0 s
E = -1.1 V
a1
50nm
t = 40 s,
E = -1.16 V
a2
50nm
t = 80 s
E = -1.17 V
a3
50nm
t = 120 s
E = -1.19 V
a4
50nm
t = 160 s
E = -1.20 V
a5
50nm
b
Silicon nitride window
Silicon nitride window
Top EC-chip with electrode
Electrolyte inlet
O-ring
Bottom EC-chip
Electrolyte outlet
2.6 nm
3.0 nm
3.0 nm
Distance (nm)
Distance (nm)
Distance (nm)
Distance (nm)
Distance (nm)
Counter electrode
Working electrode
Reference electrode
Silicon nitride window
c1
0 s
c2
10 s
c3
50 s
d1
150 s
d2
600 s
d3
3600 s
e1
e2
200
110
[00$\bar{1}$]
e3
0.21 nm
0.30 nm
f
0.0 s
2.0 s
0.4 s
6.0 s
0.8 s
10.0 s
g
32 s
8 s
40 s
16 s
48 s
0.1 μm

Figure 6

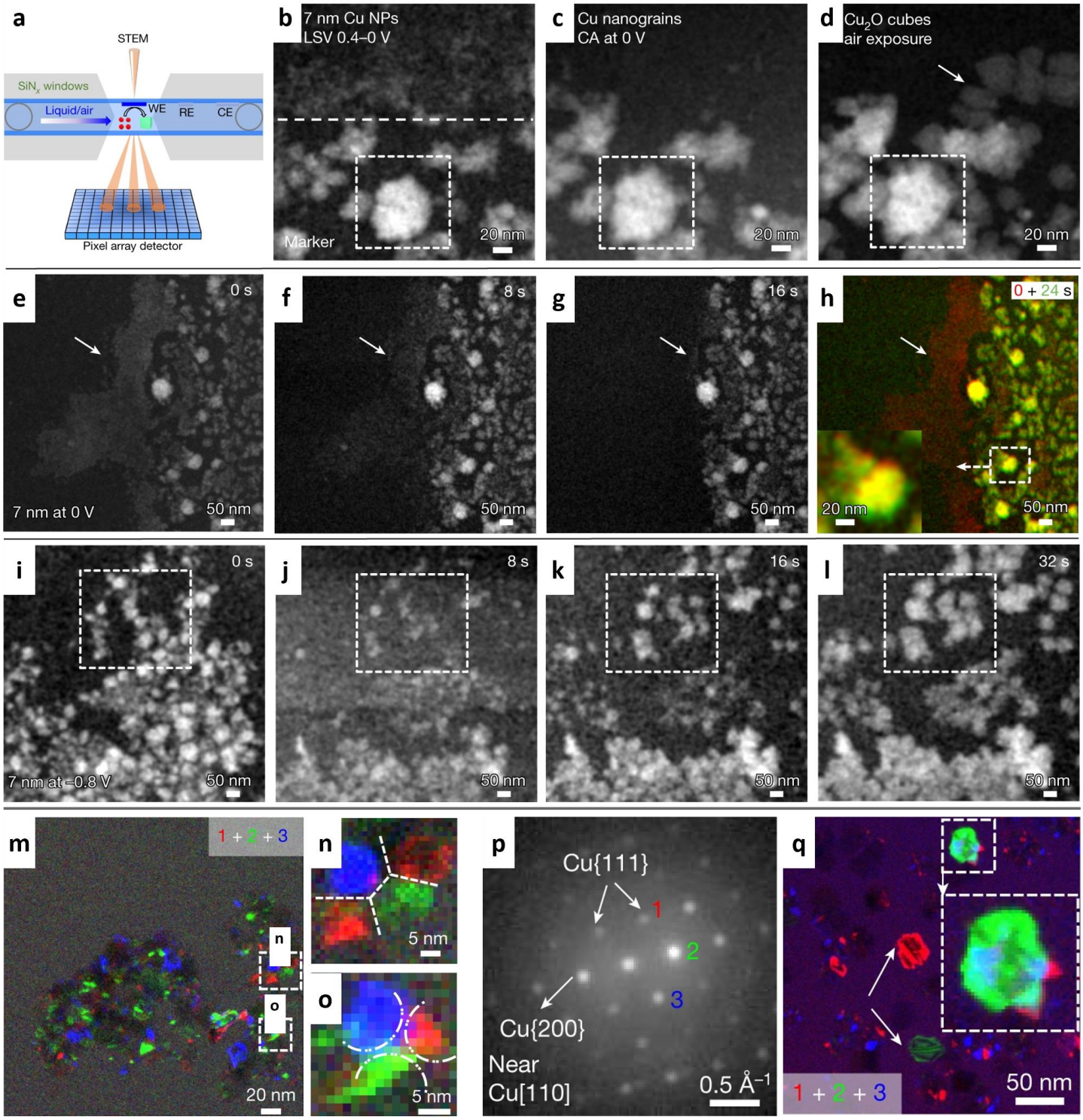
a
STEM
SiNx windows
Liquid/air
WE
RE
CE
Pixel array detector
b
7 nm Cu NPs
LSV 0.4–0 V
Marker
20 nm
c
Cu nanograins
CA at 0 V
20 nm
d
Cu2O cubes
air exposure
20 nm
e
0 s
7 nm at 0 V
50 nm
f
8 s
50 nm
g
16 s
50 nm
h
0 + 24 s
20 nm
50 nm
i
0 s
7 nm at –0.8 V
50 nm
j
8 s
50 nm
k
16 s
50 nm
l
32 s
50 nm
m
1 + 2 + 3
n
o
20 nm
n
5 nm
o
5 nm
p
Cu{111}
1
2
3
Cu{200}
Near
Cu[110]
0.5 Å–1
q
1 + 2 + 3
50 nm

Figure 7

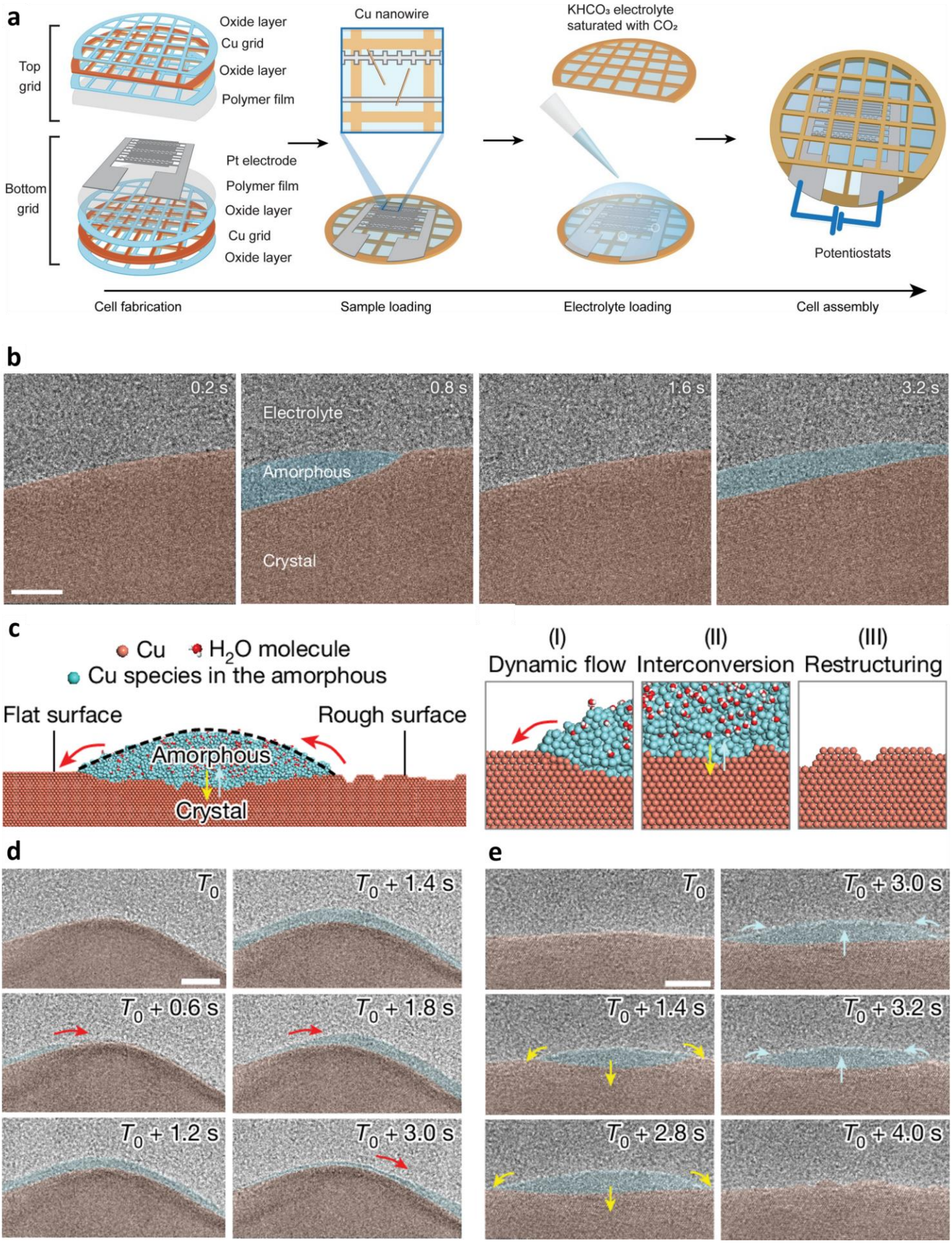
a
Top grid
Oxide layer
Cu grid
Oxide layer
Polymer film
Bottom grid
Pt electrode
Polymer film
Oxide layer
Cu grid
Oxide layer
Cu nanowire
KHCO₃ electrolyte saturated with CO₂
Potentiostats
Cell fabrication
Sample loading
Electrolyte loading
Cell assembly
b
0.2 s
0.8 s
Electrolyte
Amorphous
Crystal
1.6 s
3.2 s
c
Cu
H2O molecule
Cu species in the amorphous
Flat surface
Rough surface
Amorphous
Crystal
(I)
Dynamic flow
(II)
Interconversion
(III)
Restructuring
d
T0
T0 + 1.4 s
T0 + 0.6 s
T0 + 1.8 s
T0 + 1.2 s
T0 + 3.0 s
e
T0
T0 + 3.0 s
T0 + 1.4 s
T0 + 3.2 s
T0 + 2.8 s
T0 + 4.0 s

Figure 8

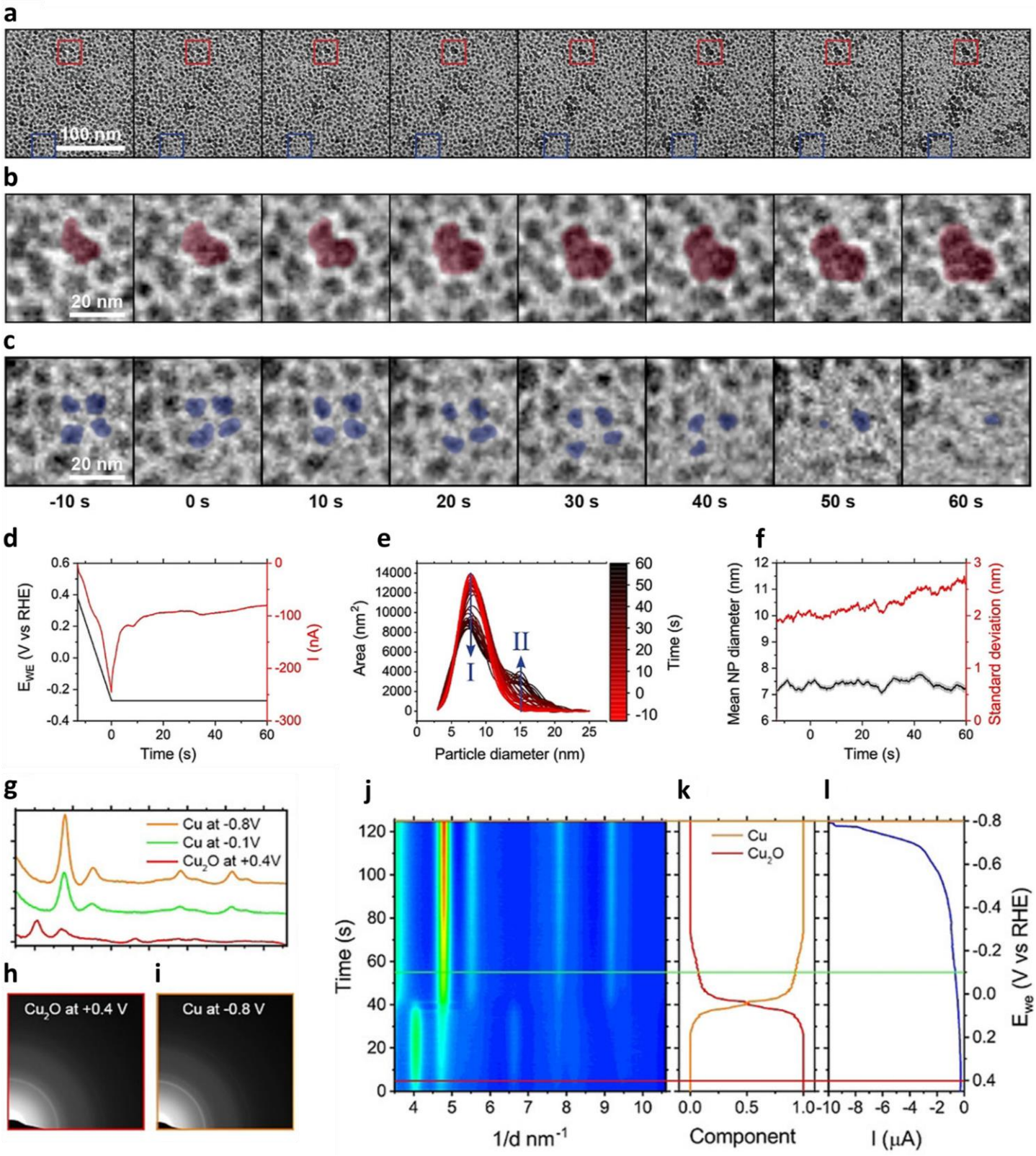
a
100 nm
b
20 nm
c
20 nm
-10 s
0 s
10 s
20 s
30 s
40 s
50 s
60 s
d
E_WE (V vs RHE)
I (nA)
Time (s)
e
Area (nm²)
Time (s)
Particle diameter (nm)
I
II
f
Mean NP diameter (nm)
Standard deviation (nm)
Time (s)
g
Cu at -0.8V
Cu at -0.1V
Cu2O at +0.4V
h
Cu2O at +0.4 V
i
Cu at -0.8 V
j
Time (s)
1/d nm-1
k
Cu
Cu2O
Component
l
I (μA)
Ewe (V vs RHE)

Figure 9

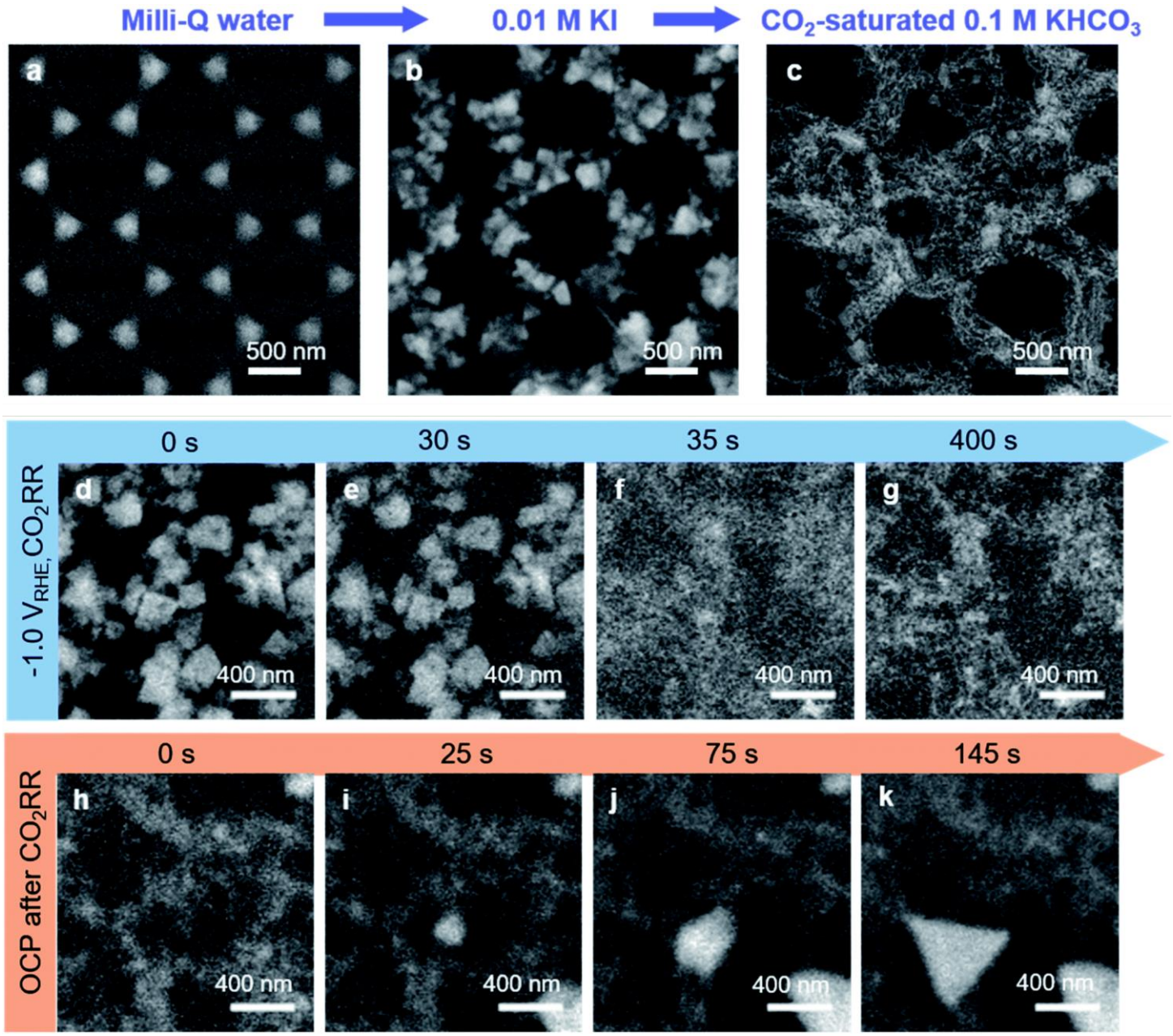
Milli-Q water
0.01 M KI
CO2-saturated 0.1 M KHCO3
a
b
c
500 nm
500 nm
500 nm
0 s
30 s
35 s
400 s
-1.0 VRHE, CO2RR
d
e
f
g
400 nm
400 nm
400 nm
400 nm
0 s
25 s
75 s
145 s
OCP after CO2RR
h
i
j
k
400 nm
400 nm
400 nm
400 nm

Figure 10

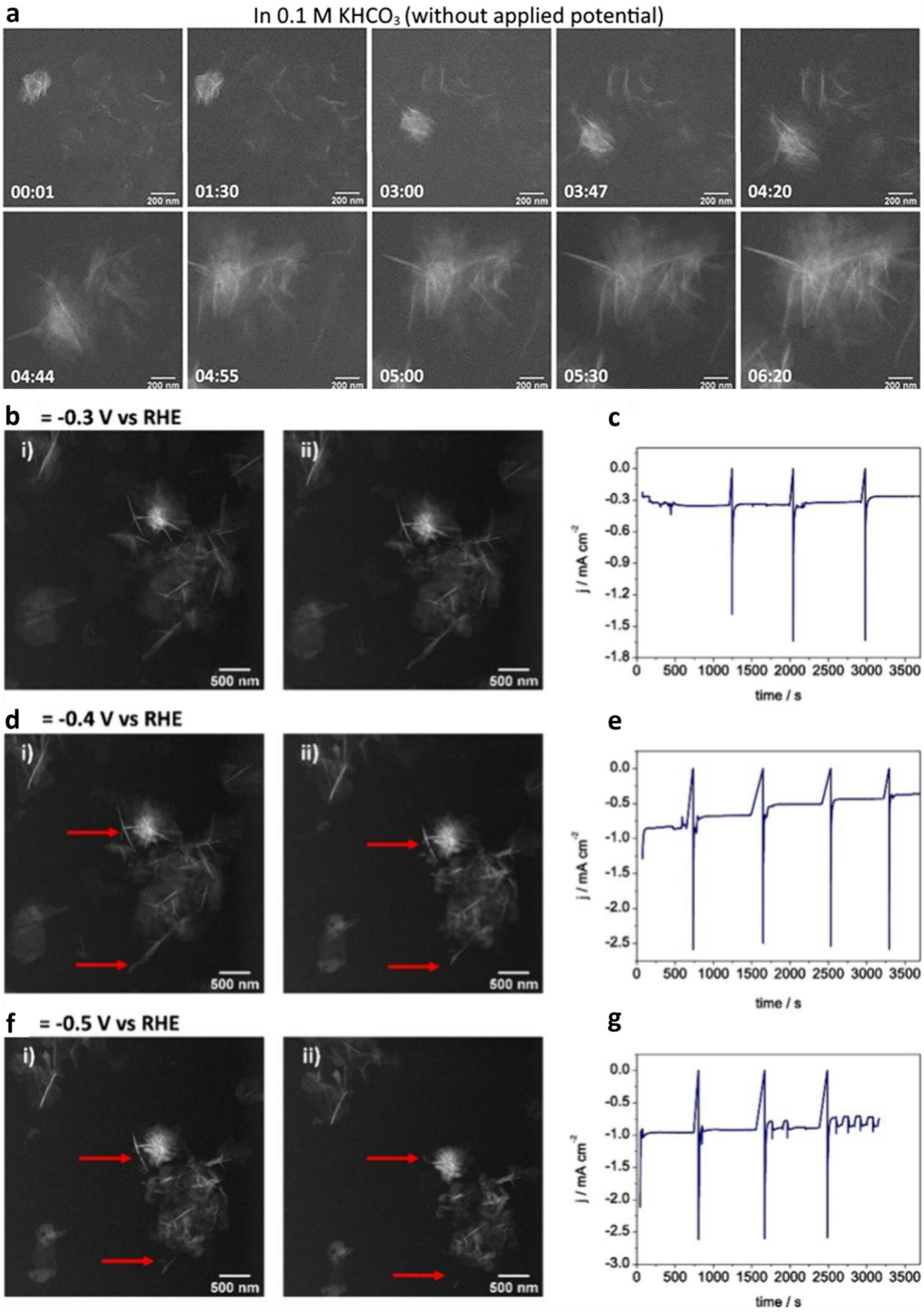
a
In 0.1 M KHCO3 (without applied potential)
00:01
01:30
03:00
03:47
04:20
04:44
04:55
05:00
05:30
06:20
200 nm
b = -0.3 V vs RHE
i)
ii)
500 nm
c
j / mA cm-2
time / s
d = -0.4 V vs RHE
e
f = -0.5 V vs RHE
g